



HAL
open science

**PROGRESSIVE STRAIN LOCALIZATION AND
FLUID-ASSISTED DEFORMATION IN MANTLE
EXHUMATION DURING RIFTING:
PETROSTRUCTURAL CONSTRAINTS FROM THE
ZABARGAD PERIDOTITES, RED SEA**

Marialine Chardelin, Andrea Tommasi, Jose Alberto Padron Navarta

► **To cite this version:**

Marialine Chardelin, Andrea Tommasi, Jose Alberto Padron Navarta. PROGRESSIVE STRAIN LOCALIZATION AND FLUID-ASSISTED DEFORMATION IN MANTLE EXHUMATION DURING RIFTING: PETROSTRUCTURAL CONSTRAINTS FROM THE ZABARGAD PERIDOTITES, RED SEA. 2023. hal-04387529v1

HAL Id: hal-04387529

<https://hal.science/hal-04387529v1>

Preprint submitted on 11 Jan 2024 (v1), last revised 9 Aug 2024 (v3)

HAL is a multi-disciplinary open access archive for the deposit and dissemination of scientific research documents, whether they are published or not. The documents may come from teaching and research institutions in France or abroad, or from public or private research centers.

L'archive ouverte pluridisciplinaire **HAL**, est destinée au dépôt et à la diffusion de documents scientifiques de niveau recherche, publiés ou non, émanant des établissements d'enseignement et de recherche français ou étrangers, des laboratoires publics ou privés.



Draft Manuscript for Review

PROGRESSIVE STRAIN LOCALIZATION AND FLUID-ASSISTED DEFORMATION IN MANTLE EXHUMATION DURING RIFTING: PETROSTRUCTURAL CONSTRAINTS FROM THE ZABARGAD PERIDOTITES, RED SEA

Journal:	<i>Journal of Petrology</i>
Manuscript ID	JPET-Dec-23-0204
Manuscript Type:	Original Manuscript
Date Submitted by the Author:	27-Dec-2023
Complete List of Authors:	Chardelin, Marialine; CNRS, Géosciences Montpellier Tommasi, Andrea; Université de Montpellier 2 and UMR5243 CNRS, Géoscience Montpellier Padron Navarta, José-Alberto; Consejo Superior de Investigaciones Científicas, Instituto Andaluz de Ciencias de la Tierra
Keyword:	Extensional shear zones, mantle exhumation, olivine deformation, fluid-assisted deformation, thermodynamic modeling
Journal of Petrology now offers Virtual Collections of published papers. You may choose up to three collections from the list below. Virtual collections will increase the visibility of your work.:	Intracontinental Rifts < Province Themes, Mantle Composition and Evolution < Process Themes, Thermodynamic Modelling

SCHOLARONE™
Manuscripts

PROGRESSIVE STRAIN LOCALIZATION AND FLUID-ASSISTED DEFORMATION IN MANTLE EXHUMATION DURING RIFTING: PETROSTRUCTURAL CONSTRAINTS FROM THE ZABARGAD PERIDOTITES, RED SEA)

Marialine Chardelin¹, Andréa Tommasi^{1*}, and José Alberto Padrón-Navarta^{1,2}

¹ *Géosciences Montpellier, CNRS & Université de Montpellier, F-34095 Montpellier, France*

² *Instituto Andaluz de Ciencias de la Tierra, CSIC, Granada, Spain*

**corresponding author: andrea.tommasi@umontpellier.fr*

ABSTRACT

The three peridotite massifs in the Zabargad island (northern Red Sea) document the exhumation of the mantle during continental rifting and the rift to drift transition. Deformation evolved from pervasive at the massif scale to localized in metric shear zones. To characterize the active processes and the role of melts and aqueous fluids in the deformation, we performed a petrostructural study of 40 samples representative of the different stages of deformation in the three massifs. Microstructures recording synkinematic crystallization of plagioclase, clinopyroxene, and orthopyroxene in the southern and amphibole-bearing spinel-websterite layers in the central and northern massifs indicate that pervasive deformation occurred in the presence of melts, but at lower pressure in the south. In the shear zones, deformation was accommodated by concomitant dislocation and dissolution-precipitation creep. Evolution from protomylonites to ultramylonites produced increasing volumes of a fine-grained polymineralic matrix where amphibole progressively replaces plagioclase and clinopyroxene. Fluid-assisted deformation at all stages is attested by the interstitial shapes of pyroxene neoblasts intermixed with olivine in the matrix. Local deformation at the brittle-ductile transition is accompanied by the crystallization of scapolite. Thermobarometry and thermodynamic modelling constrained by the microstructural observations document shearing under decreasing pressure and temperature from near solidus conditions at >1 GPa in the north and central massifs and ~0.7 GPa in the southern massif to < 600°C and <0.3 GPa in all three massifs. These data also imply increasing hydration, indicating fluid focusing and local aqueous fluid saturation in the shear zones, with sea water ingression to >10 km depth. However, fluid supply was spatially heterogeneous and probably intermittent, with equilibrium only achieved locally in the ultramylonites. The present study documents therefore how progressive strain localization and fluid-focusing in extensional shear zones enable thinning and exhumation of the mantle during continental rift and rift-to-drift transition.

INTRODUCTION

The processes thinning the lithosphere and more specifically its mantle section until complete breakup of a plate and creation of a new divergent plate boundary are still poorly understood. Traditionally, continental rifting models range between symmetric pure shear and asymmetric simple shear end-members (McKenzie 1978; Wernicke 1981). Yet, independently of the symmetry or asymmetry of the rift system as a whole, geological and geophysical data on continental margins, in particular those exposing mantle rocks at the ocean bottom, favour deformation accommodated by large-scale extensional shear zones as the most effective process for thinning the lithosphere (e.g., Boillot et al. 1987; Whitmarsh et al. 2001; Dean et al. 2015). Numerical models that successfully reproduce the geometry of continental margins also generally show mantle thinning and asthenospheric upwelling in response to localized shear deformation in translithospheric extensional shear zones (e.g., Weinberg et al. 2007; Brune et al. 2023). However, we lack knowledge on the actual geometry of these shear zones in the mantle and on the processes controlling their nucleation and growth. The role of melts and fluids on the thinning of the lithosphere and exhumation of the deep levels of the lithosphere during continental rifting and at the transition from rifting to drifting also remains a widely debated question.

The three peridotite massifs that outcrop in Zabargad (23° 36' 35" N, 36° 11' 45" E), a small (3 km²) island located within the Zabargad fracture zone, 50 km east of the axis of the Red Sea (Figure 1), offer an exceptional opportunity to document the evolution of the deformation of the mantle during the last stages of continental rifting. These peridotite massifs preserve a complete record of the deformation processes and metamorphic and metasomatic reactions involved in the exhumation of mantle slices to very shallow, near seafloor depths (Bonatti et al. 1986; Nicolas et al. 1987; Piccardo et al. 1988). The central and northern massifs are mainly composed of spinel lherzolites, whereas the southern massif is dominantly composed of plagioclase lherzolites (Bonatti et al. 1983, 1986; Nicolas et al. 1987), indicating evolution along different pressure-temperature paths.

Structural mapping and microstructural analysis document that all three massifs are characterized by pervasive foliations and lineations formed under high-temperature conditions, which are overprinted by lower temperature deformation focused in discrete shear zones tens of meters to tens of centimetre wide (Bonatti et al. 1986; Nicolas et al. 1987). The mylonitic foliations in the shear zones are in general slightly oblique to the high-temperature ones (Figure 1). Both the pervasive and mylonitic foliations have in all three massifs a general NNW to WNW trend, but dip steeply towards the SW in the central and northern massifs and variably towards the NE in the southern massif (Figure 1). Lineations also have contrasted orientations in the central and northern massifs, where they plunge shallowly towards the E, and in the southern massif, where they have variable plunges towards the NW (Figure 1). These studies also documented the development of amphibole-rich peridotites within the shear zones. Moreover, the Central and North peridotite massifs (Figure 1) are in direct contact with amphibolite to granulite facies gneisses interpreted as slivers of the thinned continental lower crust and, at the southern limit of the Central massif, the gneisses and peridotites were co-deformed (Boudier et al. 1988; Boullier et al. 1997; Seyler and Bonatti 1988).

Petrological and geochemical studies (Agrinier et al. 1993; Bonatti et al. 1986; Dupuis et al. 1993; Piccardo et al. 1998) corroborated evolution under decreasing pressures and temperatures. These studies also documented: (i) petrological evidence for melt impregnation, but depleted LREE patterns in plagioclase peridotites of the southern massif outside the shear zones, (ii) diffuse websteritic layering, flat REE patterns in peridotites, and rare Ti-rich pargasite in both peridotites and pyroxenites indicating variable degrees of metasomatism by alkalic basalts in coarse-grained peridotites of the central and northern massifs, and (iii) marked enrichment in amphiboles with variable major elements and isotopic compositions and strong LREE enrichment of the peridotites indicating metasomatism by aqueous fluids in the shear zones in all three massifs, with increasing contribution of sea-water in the later stages of deformation.

In the present study, we make use of the major advances in the analysis of microstructures brought by the development of automated high-resolution cartography of crystallographic orientations by Electron BackScattered Diffraction (EBSD), as well as of recent developments in barometry of plagioclase-bearing peridotites (Fumagalli et al. 2017) and in thermodynamic modelling of anhydrous and hydrous melting and subsolidus phase relations in peridotitic compositions (Holland et al. 2018, Jennings et al. 2015, Tomlinson and Holland 2021), to better constrain the deformation processes and feedbacks between deformation, melts, and fluids at the different stages of mantle thinning and exhumation recorded in the Zabargad peridotites.

METHODS

We performed a detailed petrostructural study of 40 samples derived from the three massifs (Figure 1 and Table 1). The samples are part of the collection of Geosciences Montpellier. They were collected by Françoise Boudier and Adolphe Nicolas during field trips in 1985 and 1986, who also performed the first microstructural analyses of the entire collection (Nicolas et al. 1985; 1987). Previous studies have analysed the amphiboles composition, whole-rock Sr, H, and O isotopes (Agrinier et al. 1993), and whole-rock trace-element compositions (Dupuy et al. 1991) of part of this collection, including some of the samples studied here.

The microstructures of all samples were analysed by optical microscopy and by cartography of the crystal orientations by electron backscattered diffraction (EBSD) at the thin section scale. For 12 samples, we also performed simultaneous high-resolution EBSD and chemical mapping by dispersive electron spectroscopy (EDS) of selected areas. Chemical compositions of the major rock-forming minerals were measured by electron microprobe analysis (EPMA) for 18 samples representative of the different microstructures and modal compositions in the three massifs.

EBSD data acquisition and processing

Mapping of crystallographic orientations of olivine, pyroxenes, plagioclase, spinel and amphibole was performed by indexing backscattered electron diffraction (EBSD) patterns in the Geosciences Montpellier SEM-EBSD facility. EBSD mapping was performed on entire

thin sections (at least 90% of the section surface was analyzed) with steps ranging from 7 to 44 microns depending on the average grain size (in all cases, most grains are covered by at least 3 data points) using a JEOL5600 scanning electron microscope equipped with a Nordlys II EBSD detector and the AZtecHKL software from Oxford Instruments. Data were acquired with a working distance of 24 mm, a beam current of 10 nA, and an acceleration voltage of 17 kV. For 12 samples representative of the different microstructural groups, higher spatial resolution EBSD and energy-dispersive X-ray spectroscopy (EDS) chemical maps with step sizes of 1 to 12.5 microns were acquired using a field-emission scanning electron microscope – the Camscan Crystal Probe X500 FE, equipped with the Oxford Symmetry EBSD detector and an UltimMax 100 EDS detector. The phases declared for EBSD indexation were: olivine, orthopyroxene, clinopyroxene, spinel, plagioclase, and amphibole (pargasite). In the high-resolution analyses, antigorite, chlorite, calcite, and talc were added to the mineral phase list. The EBSD data was cleaned by removing wild spikes (isolated measurement points) and replacing the unindexed pixels with the average orientation of their neighbours if at least 6 neighbours belonged to the same phase and had a consistent orientation.

EBSD data treatment was performed using the MTEX toolbox v.5.10.2 in Matlab (<http://mtex-toolbox.github.io/>; Bachmann et al., 2010, 2011). Grains were reconstructed using a Voronoi tessellation constrained by the indexed points and a misorientation threshold of 15° to define a grain boundary. Subgrain boundaries are defined with a misorientation threshold of 2°, considering a maximum angular uncertainty in the EBSD data of 1°. Modal compositions were approached as the area fraction occupied by each mineral on the EBSD maps. For better visualization of the microstructures, modal composition and orientation maps are presented in the following with all indexed data, but statistical analysis of the microstructure and crystallographic orientation was performed after removing grains composed of less than three pixels.

Orientation distribution functions (ODF) describing the crystal-preferred orientations of all minerals were calculated using a “de la Vallée Poussin” kernel with a half-width of 10°. They are displayed as pole figures, presented as lower hemisphere stereographic projections. The orientation of the main crystallographic directions: [100], [010] and [001] of each mineral phase is plotted relative to the principal axes of the strain ellipsoid X, Y, and Z. In some samples the orientation of the foliation and lineation could not be defined.

The concentration (intensity) of the CPO of the different minerals was quantified using the dimensionless J-index, which is the volume-averaged integral of the squared orientation densities in the ODF (Bunge, 1982). The J-index varies from 1 for a uniform orientation distribution, to infinity for a single crystal. In naturally deformed peridotites, the J-index calculated using the same parameters as in the present study typically ranges between 1 (random CPO) and 18, with a median at 4.8 (Tommasi and Vauchez, 2015). The symmetry of the olivine CPO is characterized using the BA-index, which varies between 0 and 1 (Mainprice et al, 2014). The BA-index allows a classification of the olivine CPO symmetry into 3 types: axial-[010], characterized by a point concentration of [010] and a girdle distribution of [100] (BA-index<0.35), orthorhombic, characterized by point concentrations of both [100] and [010]

($0.35 < \text{BA-index} < 0.65$), and axial-[100], characterized by a point concentration of [100] and a girdle distribution of [010] ($\text{BA-index} > 0.65$).

Intragranular misorientations, which result essentially from the accumulation of geometrically necessary dislocations, are quantified using the Kernel Average Misorientation (KAM, which is a measure of the mean misorientation around a measurement point), the local misorientation relative to the mean orientation of the grain (Mis2Mean), and the Grain Orientation Spread (GOS, which is the average of the local misorientations relative to the mean orientation of the grain). These data, together with grain sizes and shapes, are the basis for the quantitative analysis of the microstructures. Grains were classified as porphyroclasts (grains predating the deformation) or neoblasts (newly formed grains) based on both their size and internal deformation. The justification for these criteria is that both recrystallization and reactions create new grains (neoblasts) with initially small sizes and very low dislocation densities. Neoblasts are therefore defined as having a $\text{GOS} < 1^\circ$ and an equivalent grain diameter (the diameter of a circle with the same area as the grain) $< 400 \mu\text{m}$ (Figure 2). This double threshold assumes that coarse grains with low GOS values are porphyroclasts poorly oriented to deform by dislocation creep. Amphiboles being a secondary phase in the present rock assemblages, they were classified as neoblasts independently of their GOS or grain size.

To establish a quantitative characterization of the microstructure, we calculated, for each mineral, average values at the thin section scale of the orientation data (J- and BA-indexes, KAM, Mis2Mean, and GOS), as well as area-weighted averages of the equivalent grain size (diameter of a circle with the same area as the grain), aspect ratio (the ratio between the long and short axis of the ellipse that best fits the grain), and shape factor (the perimeter of the grain divided by the perimeter of a circle with the same area as the grain, which increases with increasing sinuosity of the grain boundaries). These values were calculated for the entire grain population in the EBSD map and separately for the porphyroclasts and neoblasts. Paleostresses associated with the different microstructures were estimated based on the olivine recrystallized grain size using the Van de Wal et al. (1993) piezometer based on the arithmetic mean of the equivalent neoblast size of each sample using the Python script developed by M. Sanchez-Lopez with correction for the difference in stress regime between experiments and nature (https://github.com/marcoalopez/GrainSizeTools/blob/master/DOCS/_Paleopiezometry.md).

Mineral chemistry analysis and geothermometry

Major element composition of olivine, orthopyroxene, clinopyroxene, spinel, plagioclase, and amphibole were analysed in 14 samples representative of the different microstructural groups and modal composition range in the three massifs using a Cameca SX100 electron microprobe analyser (EPMA) at the University of Montpellier. Analytical conditions and the full dataset are presented in the Supporting Information Table S1.

Optical observation of microstructures and EBSD maps were used to identify the equilibrium assemblages associated with the different stages of deformation. EDS maps have been used to identify spatial variations in chemical composition and correlate them with the deformation microstructures.

Equilibrium temperatures and pressure for different microstructural assemblies have been calculated using iteratively the Ca in Opx thermometer of Brey and Köhler (1990) revised by Nimis and Grütter (2003) and the FACE barometer of Fumagalli et al (2017). For samples that do not contain plagioclase or clinopyroxene, the temperature calculation was performed using an average pressure of 0.5 GPa. Temperatures were also estimated using the Al-Cr in orthopyroxene thermometer (Witt-Eickchen and Seck, 1991). The uncertainty in the equilibrium pressure and temperature conditions due to spatial variations in the minerals composition within a sample was estimated by considering all possible combinations between core, intermediate position, rim and matrix analyses for the different minerals in each sample and presenting the results as the median with error bars indicating the dispersion (minimum and maximum values) in each petrographic class.

Thermodynamical modelling

Phase equilibria and mineral compositions were computed by Gibbs energy minimization using the PerpleX algorithm version 7.0.9 (Connolly 2005, 2009). Forward thermodynamic modelling was performed in the KNCFMASHTOCr system using oxide and O₂ as thermodynamic system components (K₂O-Na₂O-CaO-FeO-MgO-Al₂O₃-SiO₂-H₂O-TiO₂-O₂-Cr₂O₃). Thermodynamic data for end members are defined based on Holland and Powell (2011). The considered solid solutions models were: olivine (Ol), orthopyroxene (Opx), clinopyroxene (Cpx), garnet (Gt), spinel (Spl) from (Tomlinson and Holland, 2021), plagioclase (Pl) from Holland et al. (2021), clinoamphibole from Green et al. (2016), chlorite (Chl) from White et al. (2014) with the fclin3 endmember excluded, peridotitic dry melt from Jenning and Holland (2015), and generic hydrous melt from Holland et al. (2018).

RESULTS

Microstructural groups

Based on field observations, Bonatti et al. (1986) and Nicolas et al. (1987) proposed that the three massifs recorded deformation with progressive strain localization, which allowed the preservation of a record of deformation under decreasing pressure and temperature conditions. To describe this evolution, we classified the microstructures of the peridotites into four groups (Figure 3). The first: **coarse-porphyroclastic peridotites**, is composed of peridotites with microstructures typical of deformation at high temperature and low stress conditions. It corresponds to the pervasive structuration of the massifs. The three other microstructural groups record increasing reworking of the primary coarse-porphyroclastic microstructure within the shear zones under lower temperature conditions: **protomylonites**, **mylonites**, and **ultramylonites**.

Deformation facies are usually defined based on the proportion of neoblasts of all minerals in a rock. However, in the present study the classification of the microstructures of the peridotites has been defined solely based on the microstructure of olivine (Figure 3), because,

as discussed later, the evolution of the microstructure of the other major rock-forming minerals was affected by synkinematic reactions with melts or fluids. Peridotites in which more than 50% of the olivine surface area is recrystallized are classified as **ultramylonites** and between 50 and 20 % as **mylonites**. When less than 20 % of the olivine is recrystallized, they are classified as **coarse-porphyroclastic peridotites** if the area-weighted equivalent grain diameter of the olivine neoblasts is larger than 100 microns, or **protomylonites**, if the area-weighted equivalent grain diameter of neoblasts is lower than 100 microns, suggesting incipient recrystallization under higher stress conditions. The pyroxenites were classified using the recrystallized fraction of all minerals in the thin section.

Modal compositions

Very fertile compositions, characterized by > 20 area % of Al-rich phases (clinopyroxene, plagioclase, spinel, or amphibole), predominate in all three massifs independently of the deformation microstructure (Figure 4, Supplementary Material Figure S1). Modal compositions vary almost continuously between peridotites and pyroxenites (Figure 4). Some of the studied samples are heterogeneous, containing diffuse pyroxenitic or troctolitic layers at the mm to cm scale. Yet, some samples with compositions intermediate between that of a peridotite and an igneous rock are homogeneous at the thin section scale, the heterogeneity in composition occurring at the outcrop (tens of cm to meters) scale.

In the North and Center massifs, the pyroxenites are spinel-websterites and the Al-rich phases in both peridotites and pyroxenites are clinopyroxene and amphibole. Plagioclase is only occasionally observed rimming spinel. High contents of plagioclase (up to 14 area %, Table 1) are only observed in the southern massif, where plagioclase is often the dominant Al-rich phase (Figures 4, 5a,e, 6a). In this massif, the mafic layers have gabbroic to troctolitic compositions (Figure 6d).

Amphibole-rich peridotites have dominantly mylonitic to ultramylonitic microstructures (Figures 4 and 5g,i, Table 1). Coarse-porphyroclastic peridotites have in general very low amphibole contents (Figure 4, Table 1). High amphibole contents can be, nevertheless, observed in the vicinity (within a few mm or even cm) of fractures that crosscut at variable angles the ductile foliation in samples from all microstructural groups (Figure 6d).

Microstructures

We describe below the main characteristics of each microstructural group, but the evolution of the microstructure is continuous (Figure 3) and many samples have microstructures intermediate between those described.

Microstructural groups

Coarse-porphyroclastic peridotites are dominantly composed of coarse olivine, orthopyroxene, clinopyroxene, variable amounts of plagioclase (in the southern massif only), and minor spinel and amphibole (Figure 5a, 6a). Olivine and orthopyroxene porphyroclasts are

up to 5 mm, but most often 1-2 mm wide (Figures 5a,b, 6a), while clinopyroxene and plagioclase are usually smaller than 2 mm. Coarse-porphyroclastic peridotites from the southern massif show a clear foliation and lineation marked by a shape preferred orientation (SPO) of elongated olivine and plagioclase grains (Figure 5a, 6a). Coarse-porphyroclastic peridotites from the center and northern massifs have a much weaker olivine SPO (more polygonal shapes and lower aspect ratios, Figure 6b). They have, by consequence, a weaker foliation, but the latter is often underlined by websterite layers with diffuse contacts with the peridotite and thicknesses ranging from a few mm to tens of cm (Figure 6b). Olivine-olivine grain boundaries are more sinuous in the southern massif (compare Figures 5a and 6a to 6b). In coarse-porphyroclastic peridotites from all three massifs, olivine grains have well-developed sub-structures, characterized by widely-spaced subgrain boundaries with strong misorientations at high angle to the grain elongation (Figure 7a,b). Olivine grain sizes have a multimodal distribution (Supplementary Material Figure S3) and the neoblasts, which are on average coarser than 100 μm (Figure 3), may only be separated from porphyroclasts based on their lower intragranular misorientation.

In coarse-porphyroclastic peridotites of all three massifs, coarse orthopyroxene grains have variable sizes, very irregular shapes, with embayments filled by olivine, and no shape-preferred orientation (Figures 5a,b, 6a,b). Coarse orthopyroxene grains often display undulose extinction (Figures 5b and 7a,b), but their intragranular misorientation is systematically lower than that of olivine. Smaller orthopyroxene grains have interstitial shapes with cusp-like terminations or film-like habitus along olivine-olivine grain boundaries (Figures 5a,b and 6a,b). Sometimes the film-like orthopyroxene grains are in continuity with coarse ones (Figures 6a,b). Clinopyroxenes have smaller sizes, but similar shapes as the orthopyroxenes (Figures 5a and 6a,b). Both ortho- and clinopyroxene grain boundaries are usually more sinuous in coarse-porphyroclastic peridotites from the southern massif (compare Figures 6a and 6b). In coarse-porphyroclastic peridotites from the southern massif, irregularly-shaped clinopyroxene grains tend to form trails parallel to the foliation (Figure 5a), whereas in coarse-porphyroclastic peridotites from the center and northern massif, clinopyroxene is more evenly distributed (Figure 6b).

In coarse-porphyroclastic peridotites of the southern massif, plagioclase occurs mainly as elongated grains, 1 or 2 mm long, with interstitial shapes, but a well-defined SPO marking the foliation and lineation, or in aggregates of smaller grains with rounded shapes rimming spinel (Figures 5a, 6a). In coarse-porphyroclastic peridotites of the northern and center massifs, plagioclase is usually absent, but it may occur locally as tiny grains rimming spinel (Figure 6b). Spinel occurs as coarse light-brown grains in association or not with pyroxenes. In the southern massif, it is often elongated parallel to the lineation, despite its irregular shapes, and systematically rimmed by plagioclase aggregates (Figure 5a). In coarse-porphyroclastic peridotites of the northern and center massifs, spinel has more rounded shapes and is usually associated with pyroxenes (Figure 6b). Amphibole is always minor. In coarse-porphyroclastic peridotites of the northern and center massifs, it occurs as mm-sized grains associated with clinopyroxene in the peridotites and as interstitial grains in the pyroxenite layers (Figure 6b).

In coarse-porphyroclastic peridotites of the southern massif, amphibole is rare, but may occur rimming plagioclase (Figure 6a).

The **protomylonites** (external domains of the localized shear zones) are characterized by the development of seams of a very fine-grained matrix forming a discontinuous losangular to anastomosed network at $\pm 15^\circ$ on average to the elongation of the olivine porphyroclasts (Figures 5c,d and 6c). The fine-grained matrix is composed mainly of neoblasts of olivine with average grain sizes between 25 and 100 μm (Figure 3), but it also locally contains significant amounts of fine-grained orthopyroxene or clinopyroxene neoblasts (Figure 6c). Olivine porphyroclasts are on average smaller and display more sinuous grain boundaries than in coarse-porphyroclastic peridotites (Figures 5c,d and 6c). They have a well-developed sub-structure, characterized by strong undulose extinction (Figure 5d) and a high density of subgrain boundaries with strong misorientations at high angle to the grain elongation (Figure 7c,d), and sutured grain boundaries (Figures 5c,d, 6b). As in coarse-porphyroclastic peridotites, orthopyroxene neoblasts have interstitial or film-like shapes, but they are significantly smaller (60-80 μm , Figure 3b) and tend to form asymmetric trails departing from the porphyroclasts (Figure 5c, 6c). Clinopyroxene is smaller than orthopyroxene, but has a similar habitus (Figures 5c, 6c). Plagioclase is on average smaller, but displays a similar habitus than in the coarse-porphyroclastic peridotites. Both clinopyroxene and plagioclase aggregates form trails that contribute to define the foliation and lineation. Spinel occurs both as coarse grains rimmed by spinel and tiny grains dispersed in the matrix (Figures 5c, 6c). Amphibole is rare, but may locally replace clinopyroxene and plagioclase in the fine-grained matrix network (Figure 5c). In the present sampling, this microstructural group is best expressed in the southern massif (Figures 1 and 2).

The **mylonites** (Figures 5e, f, g, h) are characterized by an increase in the fine-grained matrix fraction (Figure 3) and a decrease in the size of the porphyroclasts. The average size of the olivine neoblasts also tends to decrease, but it shows no clear correlation with the olivine neoblast fraction (Figure 2). The fine-grained matrix forms a continuous anastomosed network that encloses polycrystalline lenses up to 5 mm long, which preserve the microstructural record of the previous deformation steps (Figures 5e, f, g, h, and 9a). The anastomosed matrix network together with the SPO of olivine porphyroclasts, as well as olivine and plagioclase aggregates, define a strong foliation and lineation (Figures 5e, f, g, h, 7e-h). The fine-grained matrix is dominantly formed by intermixed olivine and orthopyroxene neoblasts (Figures 8a,c) with average grain sizes between 25 and 100 μm (Figure 3), but it also contains neoblasts of other phases in variable proportions. Neoblasts of clinopyroxene and plagioclase tend to form asymmetric trails extending from the porphyroclasts (Figures 5e, f, g, h, and 8a,c). The matrix contains higher proportions of amphibole than in the protomylonites. Orthopyroxene neoblasts have interstitial, film-like shapes along olivine-olivine grain boundaries even far away from any orthopyroxene porphyroclast; these film-like orthopyroxenes are best developed along olivine grain boundaries normal to the compression direction (Figure 8a). All phases, except amphibole, have a clear bimodal grain size distribution (Figures 5e, f, g, h, 8a,c). In mylonites of the southern massif, plagioclase has clear core and mantle structures (Figure 8c). The plagioclase rims and the neoblasts are enriched in Ca relative to the cores of the porphyroclasts,

which are more sodic (Figure 8d). In mylonites of the northern and central massifs, plagioclase occurs as small grains rimming coarse spinels and as exsolutions in clinopyroxene (Figures 8a,d). Spinel also occurs as small grains within the matrix with no plagioclase rims. In all mylonites, clinopyroxene and plagioclase are partially replaced by amphibole; for a similar recrystallized fraction, the amount of amphibole tends to be higher in the mylonites of the northern and central massifs (compare Figures 5e, g and 8a). Some mylonites of the northern massif display two generations of amphibole, which differ in grain size and Ti-content: the coarser amphiboles are enriched in Ti (Figure 8b). One mylonite of the northern massif – 85ZA51 – has a particular microstructure: it is almost entirely composed of strongly recrystallized olivine (82%), amphibole (11%), and orthopyroxene neoblasts (6%), but neoblasts of olivine and amphibole are coarser grained than in the other mylonites.

The **ultramylonites** are characterized by almost total recrystallization – the fine-grained matrix occupies on average 60-70 % of thin section surface and ≥ 50 % of the olivine fraction is composed of neoblasts (Figure 3). The matrix is essentially composed of olivine, amphibole, and orthopyroxene neoblasts, with minor clinopyroxene and spinel, and traces of plagioclase (Figures 5i,j). Most plagioclase as well as the majority of the clinopyroxene have been replaced by amphiboles. The very strong foliation is underlined by variations in the olivine and amphibole contents, with local development of mm to cm wide amphibolite layers. This fine-grained matrix encloses rather coarse, millimetric olivine porphyroclasts with ellipsoidal shapes, which have a clear SPO, well-developed subgrain structures, and recrystallization tails (Figures 5i,j 7i,h). Olivine porphyroclasts are locally rimmed or present fracture-like features filled by fine-grained orthopyroxene (Figure 5j). Orthopyroxene porphyroclasts are rare.

A single ultramylonite sample – 85ZA71-13 – displays a microstructure indicating deformation at the brittle-ductile transition. This sample contains coarse olivine porphyroclasts that are crosscut by conjugated or extensional fractures sealed by either recrystallized olivine or a very fine-grained orthopyroxene matrix (Figure 8d). These porphyroclasts are enclosed in a fine-grained matrix-rich composed of olivine-, orthopyroxene-, amphibole-, and scapolite-rich layers or lenses. The mylonitic foliation defined by these almost monomineralic recrystallized layers is anharmonically folded. The amphibole-rich layers have a bimodal grain size, enclosing locally crystals hundreds of μm wide. EDS analyses document two types of scapolite with variable Cl contents, the Cl-rich scapolites also being S-rich, which form independent layers, both containing amphibole and plagioclase clasts (Figure 8f). Plagioclase clasts are locally observed in the S-rich scapolite layers. Biotite occurs locally within the fine-grained matrix, but chlorite is not observed.

Pyroxenites

In the central and northern massifs, **pyroxenites** are spinel-websterites, which occur as diffuse layers of variable thickness. They have in general coarse-granular microstructures and are composed of millimetric, equiaxed, but irregularly shaped, intermixed ortho- and clinopyroxenes, with variable proportions of olivine crystals with very irregular shapes, minor spinel and amphibole (replacing clinopyroxene or as isolated grains with interstitial shapes), and occasionally very minor plagioclase and amphibole rimming spinel (Figure 6b). The

peridotite in the vicinity of the websterite layers display common film-like orthopyroxene grains along olivine-olivine grain boundaries (Figure 6b). Although amphibole is a primary accessory phase in most spinel-websterites, in some, like 85ZA42b, the amphibole fraction is enhanced in the vicinity of ghost conjugated fractures that crosscut the coarse-granular microstructure. In the central massif, at the contact with the gneisses (Figure 1), pyroxenite layers show ultramylonitic microstructures and have higher plagioclase or amphibole contents (Figure 3 and Table 1). In these ultramylonites, all phases, except spinel, are largely recrystallized, forming a very fine-grained matrix (grain sizes $\sim 25 \mu\text{m}$) that encloses rare orthopyroxene and clinopyroxene porphyroclasts. Olivine and plagioclase are always fine-grained. Amphibole replaces clinopyroxene and to a lesser extent plagioclase and orthopyroxene.

Samples with gabbroic to troctolitic compositions from the southern massif, like 85ZA26c or 85ZA71-12, display coarse porphyroclastic microstructures and a rough compositional layering, marked by variations in the olivine content, parallel to the foliation (Figure 6d). Plagioclase crystals have interstitial habitus. Coarse clinopyroxene crystals ($>5 \text{ mm}$ long) have thick exsolutions of orthopyroxene and plagioclase. Coarse orthopyroxene has finer clinopyroxene exsolutions. In the olivine-bearing layers, large polycrystalline lenses of plagioclase rim coarse spinel grains, with both the spinel grains and the plagioclase lenses elongated parallel to the lineation. Static replacement of clinopyroxene and plagioclase by amphibole in the vicinity of straight millimetric scale ultramylonite bands forming conjugate pairs or brittle fractures is observed in peridotites and pyroxenites with variable microstructures in all three massifs (Figure 6d).

Microstructure quantification

The evolution of the microstructure, illustrated above by representative examples, may be quantified for the entire dataset by the analysis of the area-weighted mean of the equivalent grain diameter, aspect ratio, shape factor, and mean intragranular misorientation of the olivine and orthopyroxene porphyroclasts. We based this analysis on the porphyroclasts, rather than the neoblasts, because the latter were in many cases mapped by too few measurements to be correctly described. Olivine and orthopyroxene were chosen because they are the dominant mineral phases in the peridotites. Moreover, as it will be discussed later, they represent end-members in terms of deformation processes: olivine microstructures are typical of dislocation creep and dynamic recrystallization, whereas orthopyroxene microstructures point to reactions with a liquid phase (melt or aqueous fluid).

With rare exceptions, the olivine porphyroclasts average size decreases from millimetric in the coarse-porphyroclastic peridotites to $<250 \mu\text{m}$ in the ultramylonites (Figure 9a). In contrast, the average size of the orthopyroxene porphyroclasts, which ranges from $> 2 \text{ mm}$ to $<100 \mu\text{m}$, shows a large variation from sample to sample, but no systematic decrease from coarse-porphyroclastic peridotites to protomylonites. Orthopyroxene porphyroclasts sizes decrease, however, from the protomylonites to the mylonites and ultramylonites. In most samples, the

orthopyroxene porphyroclasts are coarser than the olivine porphyroclasts. There are no systematic variations between peridotites from different massifs.

Comparison of the average aspect ratios of olivine and orthopyroxene porphyroclasts indicates that olivine is systematically more elongated than orthopyroxene (Figure 9b). However, neither olivine nor orthopyroxene shows a systematic variation of the porphyroclast average aspect ratio between the different microstructures. Olivine in the coarse-porphyroclastic peridotites of the central and northern massifs tends to be less elongated than in the southern massif. Analysis of the EBSD maps of samples representative of the different microstructures (Figure 5) shows that the elongation of olivine porphyroclasts is associated with a shape-preferred orientation (SPO), which materializes the lineation and foliation in all samples, but that in the coarse-porphyroclastic and protomylonitic peridotites, the orthopyroxenes, despite being anisometric, do not display a SPO consistent with the foliation and lineation. They have very irregular shapes and, when they show a weak SPO, the latter is oblique to the foliation.

Orthopyroxene porphyroclasts have usually more sinuous grain boundaries than olivine porphyroclasts, quantified by their higher shape factor values (Figure 9c). There is no systematic variation of the olivine porphyroclasts average shape factor between the different microstructures. There is no systematic variation of the sinuosity of orthopyroxene porphyroclasts grain boundaries between the coarse-porphyroclastic peridotites to the protomylonites, but a clear decrease from the protomylonites to the ultramylonites.

The mean average intragranular misorientation is also systematically stronger in the olivine porphyroclasts than in the orthopyroxene porphyroclasts (Figure 9d). Although there is no systematic variation of the intragranular misorientation, quantified by the GOS, between the coarse-porphyroclastic peridotites to the protomylonites, the intragranular misorientation of both olivine and orthopyroxene tends to decrease from the protomylonites to the ultramylonites. This evolution is also visible in the intragranular misorientation maps of selected samples (Figure 7), which show more saturated colour scales and more closely spaced subgrain boundaries, in particular for olivine, in the ultramylonites. In addition, within each microstructural group, the intragranular misorientation in the olivine porphyroclasts is higher in the southern massif peridotites.

Crystal preferred orientations

Olivine crystal preferred orientations (CPO) have dominantly an orthorhombic symmetry (BA-indexes between 0.35 and 0.65, Figure 10a). Coarse-porphyroclastic peridotites have, nevertheless, a stronger tendency towards axial-010 patterns (BA-indexes <5, cf. red symbols in Figure 10a). On average, the intensity of the olivine CPO (J index) decreases from the coarse-porphyroclastic peridotites to the ultramylonites. Separate analysis of the CPO of olivine porphyroclasts and neoblasts illustrates that the porphyroclasts CPO is systematically more concentrated (higher J indexes, Figure 10b) than the neoblasts CPO, indicating that recrystallization produces dispersion of the CPO. It also shows that, with few exceptions, the neoblasts CPO has lower BA-indexes than the porphyroclasts CPO, indicating that

recrystallization tends to disperse more the [100] axes than the [010] ones. Comparison of pole figures of the CPO of olivine porphyroclasts and neoblasts for a representative sample illustrates this evolution (cf. inset in Figure 10b). It also highlights the strong correlation between the porphyroclasts and neoblasts orientations, consistently with inheritance of orientation from the parent grains during dynamic recrystallization.

Figure 11 illustrates the CPO of all major rock-forming minerals in the structural reference frame for representative samples of the different microstructural facies. Despite the decrease in intensity of the CPO from the coarse-porphyroclastic peridotites to the ultramylonites (Figure 10), in all microstructural facies, the **olivine** CPO is characterized by a maximum of [100] aligned with the lineation (materialized by the elongation of olivine and plagioclase porphyroclasts) and a maximum of [010] orthogonal to the foliation plane, with, in the rare samples that have a axial-[100] CPO, some dispersion of [010] in the YZ plane. In the coarse-porphyroclastic peridotites crosscut by cm-scale diffuse spinel-websterite (northern and central massif) or gabbroic/troctolitic (southern massif) layers, the [010] maximum is normal to this layering. [001] is more dispersed and forms either a weak maximum normal to the lineation within the foliation or rough girdles in the foliation plane or normal to the lineation. Solely rare ultramylonites show a different olivine CPO, which is characterized by similar distributions of [100] and [001], with both axes displaying a weak maximum parallel to the lineation (Figure 11).

Orthopyroxene CPO is highly variable (Figure 11). In many samples, it is characterized by a maximum of [001] aligned with the lineation and the $[100]_{ol}$ maximum and a maximum of [100] perpendicular to the foliation. However, very weak orthopyroxene CPO, with secondary concentrations of [001] oblique to the lineation is also common. In addition, some mylonites and ultramylonites show weak, but clear orthopyroxene CPO characterized by a maximum of [001] normal to the foliation.

Clinopyroxene CPO is usually weaker than the olivine and orthopyroxene CPO (Figure 11). Most coarse-porphyroclastic peridotites and protomylonites display, nevertheless, some alignment of [001] parallel to the lineation and of [010] or the pole to (100) normal to the lineation. In the mylonites and ultramylonites, the clinopyroxene CPO is poorly defined, with multiple maxima due to the presence of a few porphyroclasts. In some samples, one of the [001] maxima is aligned with the lineation and the $[100]_{ol}$ maximum, but in most cases, there is no clear relation between the clinopyroxene CPO and the structural reference frame. In coarse-porphyroclastic peridotites crosscut by cm-scale diffuse spinel-websterite layers from the north and central massif, clinopyroxene in the websterite layers is characterized by either a girdle distribution of [001] in the layering plane, whereas the gabbroic or troctolitic layers in the southern massif are characterized by a concentration of $[001]_{cpx}$ at high angle to the layering.

In coarse-porphyroclastic peridotites and protomylonites, the **plagioclase** CPO is characterized by either a [001] maximum slightly oblique to the lineation and a (100) maximum parallel to the foliation or the opposite (Figure 11). In the mylonites, plagioclase CPO are weaker and characterized by a poor alignment of the normal of (010) with the lineation and of

[100] normal to the foliation. The plagioclase fraction in the mylonites of the northern and central massifs and in the ultramylonites, in general, is too low for a quantitative analysis of the CPO.

In coarse-porphyroclastic peridotites and protomylonites, the **amphibole** content is often low and its CPO is not clearly defined, displaying multiple maxima. It often mimics the cpx CPO (Figure 11). In mylonites containing significant amounts of amphibole, the amphibole CPO, which is most often weak, is characterized by a [001] maximum at a low angle or parallel the lineation and the [100] olivine maximum and concentration of (100) at a low angle to the foliation. However, in some mylonites, amphibole has a CPO characterized by a girdle distribution of [001] in the XZ structural plane, which mimics, in more dispersed, the clinopyroxene CPO (Figure 11). In amphibole-rich ultramylonites, amphibole displays a strong CPO characterized by alignment of [001] with the lineation and the [100]_{ol} maximum and of (100) with the foliation (Figure 11).

Mineral chemistry

Olivine has X_{Mg} (Mg/(Mg+Fe) apfu, atoms per formula unit) varying from 0.88 to 0.91 and Ni contents ranging from 0.0035 to 0.01 apfu in the peridotites and cm-scale pyroxenite layers in the composite samples (Figure 12a). The thicker pyroxenite 85ZA63 has significantly lower X_{Mg} (0.85-0.86) and Ni content (0.0017-0.004 apfu). Compositions, in particular Ni contents, are highly variable both among samples and within each sample, but no systematic variation between core, rims, or neoblasts within a sample or correlation with the neither the microstructural facies of the sample nor its provenance (massif) are observed. The dispersion in olivine compositions documented in the present study is consistent with previous data by Bonatti et al. (1986) and Piccardo et al. (1988).

Orthopyroxene is enstatite with X_{Mg} ranging between 0.88 and 0.91 in the peridotites and cm-scale pyroxenite layers in the composite samples and between 0.83 and 0.87 in the pyroxenite 85ZA63 (Figure 12b). As for olivine, there are no systematic variations in X_{Mg} of orthopyroxene as a function of the microstructure or provenance. In contrast, Ca contents systematically decrease from core to rim in the porphyroclasts and the neoblasts within most samples (Figure 12b). An exception is pyroxenite 85ZA63, where orthopyroxene has rather homogeneous low Ca contents, that are slightly higher in some neoblasts. Another exception is an orthopyroxene neoblast in an amphibole-domain in ultramylonite 85ZA11, which displays a high Ca content (>0.06 apfu), whereas most orthopyroxenes in this sample have Ca contents <0.01 apfu. Ca content in orthopyroxene also varies systematically with provenance: the highest Ca contents (>0.06 apfu) were measured in the cores of orthopyroxene porphyroclasts of peridotites from the southern massif. Al contents in orthopyroxene are also highly variable (from 0.005 to 0.3 apfu) and decrease rather systematically from core to rim in the porphyroclasts and the neoblasts, except for two neoblasts in ultramylonite 85ZA11 that have rather high Al contents (Figure 12c). However, in contrast to the Ca contents, the highest Al contents and most marked core-rim-neoblasts variations were measured in peridotites and pyroxenites of the Central and Northern massifs.

Clinopyroxene is diopside with X_{Mg} ranging between 0.88 and 0.95. The Al content, which varies from 0.05 to 0.3 apfu, is anticorrelated with X_{Mg} , defining three trends: a first, flatter, trend for the peridotites of the central and northern massif, a second, steeper, trend for the peridotites of the southern massif, and a third for the intergranular variability in pyroxenite 85ZA63 (Figure 12d). In the peridotites, these trends result in a systematic increase in X_{Mg} and a decrease in Al content from core to rim in the porphyroclasts and even more in the neoblasts within the individual samples. The decrease in X_{Mg} is more marked in the peridotites of the southern massif. There is no systematic variation of Cr and Ti contents in clinopyroxene with the sample provenance or microstructure; most samples have Cr contents in clinopyroxene between 0.15 and 0.04 apfu and Ti contents below 0.025 apfu (Supporting Information Table S1). However, in most samples, the Cr content in clinopyroxene decreases from core to rim in the porphyroclasts and even more in the neoblasts (Supporting Information Table S1). The present analyses are consistent with previous data by Bonnatti et al. (1986) and Piccardo et al. (1988), including the contrast in compositions between the southern massif and the central and northern massifs.

Plagioclases display an extreme variation in Al content and X_{Ca} (Ca/(Ca+Na) apfu). They range from andesine (X_{Ca} of 0.4-0.5) in peridotite and pyroxenite layers of protomylonite 86Z30 from the central massif, labradorite (X_{Ca} 0.5-0.7) in plagioclases rimming spinel in mylonites and ultramylonites in the central and northern massifs (85ZA63, 85ZA50 and 85ZA48) and cores of plagioclase porphyroclasts in protomylonites from the southern massif (85ZA37 and 85ZA36), bytownite (X_{Ca} between 0.7-0.9) in cores and rims of plagioclase porphyroclasts coarse porphyroclastic peridotites 85ZA1, protomylonites 85ZA37 and 85ZA36, and mylonite 85ZA7b from the southern massif as well as neoblasts in mylonites of the central and northern massifs, to anorthite ($X_{Ca}>0.9$) in rims and matrix grains of mylonite 85ZA7b and ultramylonite 85ZA71-13 and in coarse grains in the pyroxenitic layer in protomylonite 85ZA31c from the southern massif (Figure 12e). Both coarse porphyroclastic peridotite 85ZA1 and mylonite 85ZA7b show enrichment in X_{Ca} from core to rim (Figure 12e, Figure 6d=EDS 7b). The present analyses are consistent with previous data by Bonnatti et al. (1986) and Piccardo et al. (1988), but some plagioclases analyzed by Piccardo et al. (1988) display significantly lower Ca contents than our data (Figure 12e).

Spinel displays extreme variations in both X_{Mg} and X_{Cr} (Cr/(Cr+Al+Fe³⁺) apfu) (Figure 12f). Coarse porphyroclastic peridotites and protomylonites from the northern and central massifs display the highest X_{Mg} (~0.75) and lowest X_{Cr} (~0.1; Figure 12f). The lowest X_{Mg} (~0.25) and highest X_{Cr} (~1) is displayed by ultramylonite 85ZA51 from the northern massif. Peridotites from the southern massif show intermediate values, but also present a trend of decrease in X_{Mg} and increase in X_{Cr} with increasing localized deformation. In addition, all samples show enrichment from cores to rims to matrix in Cr and Fe. The most extreme variation (X_{Cr} 0.1-0.6, X_{Mg} 0.7-0.2) is displayed by mylonite 85ZA50 from the northern massif. Relative to the peridotites, spinels in the pyroxenite 85ZA63 are enriched in Al for a given X_{Mg} . The present analyses are consistent with those from Bonnatti et al. (1986), but we sampled a higher variability in spinel composition. Some spinels analyzed by Piccardo et al. (1988) have higher X_{Mg} .

As observed in previous studies (Bonnatti et al., 1986; Piccardo et al., 1988; Agrinier et al. 1993), **amphiboles** have a wide range of compositions, from Ti-rich pargasite to tremolite (Figure 13a = K+Na vs. Al), based on structural formula calculated following Li et al. (2022). Pargasite with < 0.2 apfu Ti occurs in coarse-porphyroclastic peridotites from the three massifs (Figure 13a, b). Synkinematic amphiboles in mylonites of the three massifs are also dominantly pargasite, but with lower Ti contents, or magnesio-hornblende, and those in ultramylonites range from Ti-poor pargasite to magnesio-hornblende with rare tremolite, marking a trend of decreasing Ti, Al^{IV} and Na+K contents with increasing low-temperature deformation (Figure 13a,b). The lowest Al^{IV} and Na+K contents are observed in amphiboles that statically replace clinopyroxenes in the vicinity of a fracture in protomylonites 85ZA41 and 85ZA31c, but on average amphiboles in 85ZA31c have higher Al^{IV} and Na+K contents. It is noteworthy that the static amphiboles in these samples show a wide range of compositions covering most of the Al^{IV} vs Na+K trend of the Zabargad data (Figure 13a). The static amphiboles in both samples have very low Ti and high Si contents, with on average lower Si contents in 85ZA31c (Figure 13b). Mylonites 85ZA48 and 85ZA45, which have two petrographically distinct generations of amphibole (cf. Figure 8b), show a strong variation in Ti (Figure 13b) and Na+K contents (Figure 13a). Synkinematic amphiboles from mylonite 85ZA51 are slightly offset from the major trend, being enriched in Na+K relative to their Al^{IV} content (Figure 13a). These amphiboles are enriched in Cr (0.35-0.4 apfu) relative to the main Zabargad amphibole population (Figure 13c). A similar offset is displayed by some analyses of amphiboles of the northern massif by Agrinier et al. (1993) and to a lesser extent by Bonatti et al. (1986) and Piccardo et al. (1988). Amphiboles from ultramylonitic pyroxenite 85ZA63, which were also previously analyzed by Agrinier et al. (1993), have highly variable compositions (Figure 13a,b,c).

Amphiboles in coarse-porphyroclastic peridotites 86Z30 and 86Z31a from the center massif and 85ZA37 from the southern massif have very low Cl contents, but coarse-porphyroclastic peridotite 85ZA1 has Ti-rich pargasite (Figure 5) with Cl contents up to 0.08 apfu (Figure 13d). In most mylonites and ultramylonites the amphiboles contain Cl (Figure 13d). In the southern massif, with increasing strain localization, the amphibole Cl content first increases to > 0.13 apfu in mylonite 85ZA7b and then decreases to 0.05-0.1 apfu in ultramylonites 85ZA11 and 85ZA71-13. Mylonites from the northern and center massifs display highly variable Cl contents, covering the entire range of observations, and no simple relation between the Cl and Si content. Cl contents in amphiboles that statically replace clinopyroxene in the vicinity of fractures are low and independent of the Si content in protomylonite 85ZA41, but high and anticorrelated with the Si content in protomylonite 85ZA31c (Figure 13d).

Equilibrium pressures et temperatures

Equilibrium temperatures have been estimated using the Al-Cr and the Ca in Opx thermometers (Figures 14a,b). Both thermometers predict a decrease in equilibrium temperature from core to rim to matrix within individual samples. They also predict a consistent decrease in equilibrium temperature with increasing localized deformation within the entire dataset, with the highest temperatures predicted for the cores of Opx porphyroclasts in the

coarse-porphyroclastic peridotites and the lowest temperatures for Opx neoblasts in the matrix of ultramylonites. However, the plot of the Al content in Opx vs. the temperatures estimated using the Al-Cr in Opx thermometer shows distinct trends for the southern and central and northern massifs (Figure 14a). For comparable Al contents lower equilibrium temperatures are predicted for the central massif. This highlights a possible effect of pressure on this system. In contrast, temperatures predicted using the Ca in Opx thermometer vs. Ca contents neatly materialize the exponential relation used to adjust the experimental data for the thermometer, indicating a lower pressure sensitivity (Figure 14b).

Despite a high variability of compositions within each sample, in most peridotites from the northern and central massifs and in coarse-porphyroclastic peridotite 85ZA37 from the southern massif, the Al^{IV} in clinopyroxene displays a rough negative correlation to the X_{Ca} of plagioclase (Figure 14c). The lowest X_{Ca} of plagioclase and the highest Al^{IV} contents in clinopyroxene were measured in cores from coarse-porphyroclastic peridotites from the central massif and the lowest values are displayed by matrix grains in mylonite 85ZA50. It is noteworthy that the cores plagioclase and clinopyroxene of coarse-porphyroclastic peridotite 85ZA37 from the southern massif have similar compositions to rims in mylonite 85ZA51 from the northern massif (Figure 14c). In contrast, in coarse-porphyroclastic peridotite 85ZA1 and mylonite 85ZA7b of the southern massif as well as mylonite 85ZA45 of the northern massif, the Al^{IV} in clinopyroxene varies strongly at roughly constant X_{Ca} of plagioclase (Figure 14c). Within each sample, despite the strong dispersion in the measurements, the median Al^{IV} in clinopyroxene decreases from core, to rims, and to matrix grains. The present data correlate well with Fumagalli et al. (2017) data for fertile compositions, which show an increase Al^{IV} in clinopyroxene (from 0.06 to 0.16) and a decrease in X_{Ca} of plagioclase (from 0.83 to 0.5) with increasing pressure from 0.3 to 0.9 GPa. The present analyses are consistent with previous data by Bonatti et al. (1986) and Piccardo et al. (1988), including the contrast in compositions between the southern massif and the central/northern ones.

The pressures calculated using the FACE barometer of Fumagalli et al. (2017) based on the temperatures estimates with the Ca in Opx thermometer imply a progressive decrease in equilibration conditions in all three massifs (Figure 14d). In the southern massif, we document both cooling and decompression associated with the localized deformation. The composition of the cores in coarse-porphyroclastic, protomylonitic, and mylonitic peridotites, as well as previous data by Bonatti et al. (1986), points to initial pressures > 0.7 GPa and temperatures ~ 1200 °C, which evolve during the localized deformation to 900-800 °C and 0.5-0.3 GPa based on rim and matrix neoblasts data. Intermediate pressures and temperatures (< 1000 °C at ~ 0.6 GPa) are recorded by the compositions of partially reequilibrated cores. The matrix data of mylonite 85ZA7b results in equilibration temperatures ~ 700 °C, but negative pressures.

In the central and northern massifs, the thermobarometric data point to almost isothermal decompression at 750-850 °C, starting at > 0.8 GPa (core and rim data in coarse porphyroclastic peridotite 86ZA30) and ending at ~ 0.2 GPa (matrix data in mylonites 85ZA45 and 85ZA63). Higher temperatures (> 900 °C) at ~ 0.8 GPa are predicted based on previous analyses by Bonatti et al. (1986) and Piccardo et al. (1988). This evolution is consistent with the equilibration conditions inferred for the gneisses co-deformed at the contact with mylonitic

peridotites of the Central massif (Figure 14d), which evolved from 1.05 GPa and 850-800°C to 700-800°C and 0.3 GPa (Boudier et al. 1988, Seyler and Bonatti 1988). In these gneisses, analysis of fluid inclusions implies further exhumation and cooling up to 0.15 GPa and 450°C (Boullier et al. 1997).

DISCUSSION

Evolution of deformation conditions and deformation processes

The present petrostructural data document the evolution of deformation processes and reactions during the exhumation of the mantle along extensional shear zones during the formation of the Red Sea rift. In the three peridotite massifs, strain localization into progressively smaller volumes (discrete shear zones) preserved a complete record of the evolution of deformation at decreasing temperature and pressure conditions. The last stages of deformation recorded in all three massifs correspond to very shallow depths (<0.3 GPa), but still elevated temperatures (>700°C, constrained by the absence of chlorite, Figures 14d and 15). However, the petrostructural record in the southern and central/northern massifs implies markedly different initial conditions. The pervasive deformation recorded in the southern massif occurred in a shallow (< 30 km depth) lithosphere-asthenosphere boundary (Figure 14), whereas the pervasive deformation in the central and northern massifs is associated with thinning of the subcontinental lithospheric mantle. Despite this difference in initial conditions, the active deformation processes and the role of melts and fluids in the different stages of mantle exhumation are similar.

Pervasive deformation – coarse-porphyroclastic microstructures

Analysis of the microstructures and CPO of the coarse-porphyroclastic peridotites indicate that the pervasive deformation in the three massifs occurred by melt-assisted dislocation creep under near solidus conditions. The coarse-porphyroclastic peridotites have a clear foliation and lineation materialized by the elongation and shape preferred-orientation of olivine crystals with strong intragranular deformation (subgrains and undulose extinction, Figures 5a,b, 9b,d) and CPO (Figures 10 and 11). Thus olivine, which is the volumetrically dominant phase forming a continuous stress-bearing framework in peridotites, deforms essentially by dislocation creep. However, (1) the parallelism between the diffuse pyroxenitic or gabbroic layering and the foliation (Figure 6) and (2) the irregular shapes of coarse orthopyroxene crystals and cusp-shaped terminations and film-like habitus of orthopyroxene crystals along olivine grain boundaries (Figures 5a,b and 6a), which record dissolution and precipitation from a liquid phase, respectively, indicate that the pervasive deformation occurred under melt-present, near solidus conditions, in all three massifs. In the southern massif peridotites, the high contents of plagioclase, which cannot result from subsolidus re-equilibration of spinel-peridotites, further point to refertilization by percolating melts (Figures 4 and 5a). The interstitial, but elongated

shape of these plagioclases as well as clinopyroxene crystals and aggregates and the fact that they show clear CPO consistent with the olivine CPO despite having low intragranular misorientations (Figures 8a,b and 11) further points to an origin by crystallization of melts coeval with the deformation. The undulose extinction and rare subgrains, but the absence of recrystallization of these melt-derived phases indicate limited pervasive deformation under subsolidus conditions.

The composition of the mafic layers indicates that the high-temperature, near-solidus deformation that formed the coarse-porphyroclastic foliation occurred in the spinel stability field in the central and northern massif, but in the plagioclase stability field in the southern massif. Thermobarometric estimates derived from cores data from coarse-porphyroclastic peridotites of the southern massif (Figure 13, 1100-1150 °C, 0.6-0.7 GPa) record equilibration at near solidus conditions at low pressure, consistently with the inferred synkinematic conditions. In contrast, thermobarometric estimates obtained using cores data from coarse-porphyroclastic peridotites of the central massif (Figure 13, ~800°C, 0.8 GPa) correspond to subsolidus conditions, implying chemical re-equilibration of these peridotites at lower temperatures and pressures after the deformation that produced the pervasive coarse-porphyroclastic fabric and pyroxenitic layering. The less sinuous pyroxene and olivine grain boundaries in the coarse-porphyroclastic peridotites and pyroxenites of the central and northern massifs (Figure 6b) further point to subsolidus re-equilibration (annealing). Both data suggest a time gap between the pervasive and localized deformations in the central and northern massif, during which the mantle volume that presently outcrops was maintained at temperatures high enough to allow for effective solid-state diffusion. This contrasts with the continuous petrological and microstructural record in the southern massif.

The olivine CPO in coarse-porphyroclastic peridotites from all three massifs records dominant activation of the [100](010) slip system (Figure 11). The moderate axial-[010] tendency (BA-index between 0.15-0.4, Figure 10) may be explained by deformation in the presence of low melt fractions (Higgie and Tommasi, 2012, 2014). The CPO of pyroxenes, which is often characterized by multiple maxima, with one coherent and others uncorrelated with the olivine CPO, implies that part of the pyroxenes formed prior to the deformation and part result from reactive melt percolation during or after the deformation. The intragranular deformation of the coarse orthopyroxene crystals corroborates their pre-deformation origin. The higher dispersion of the clinopyroxene CPO may be explained by a higher fraction of secondary, melt-derived crystals. The plagioclase CPO, which contrasts with the low intracrystalline deformation of the grains, may result from oriented crystallization in a deforming rock (Higgie and Tommasi, 2012, 2014).

Stresses associated with the pervasive deformation, based on the arithmetic mean of the equivalent neoblast sizes of olivine and the Van der Wal et al. (1993) piezometer, are on the range 50-85 MPa, with a mean at 67 MPa (Figure 15).

Localized deformation – Protomylonites, mylonites and ultramylonites

The early stages of localized deformation, which are preserved in the protomylonites that compose the external domains of the shear zones, are characterized by the development of low fractions of a very fine-grained matrix that forms a discontinuous losangular to anastomosed network at $\pm 15^\circ$ on average to the elongation of the olivine porphyroclasts (Figure 5c,d, 6c). This matrix is produced by dynamic recrystallization of olivine, as documented by the core-and-mantle structure of the olivine porphyroclasts (Figure 5c,d, 6c), but also by dissolution-precipitation processes, which are attested by the shapes of the orthopyroxene porphyroclasts and the asymmetric tails composed of intermixed fine-grained olivine-orthopyroxene that depart from them (Figure 5c,d, 6c). These dissolution-precipitation microstructures imply deformation in presence of aqueous fluids (e.g., Hidas et al. 2016) or water-rich evolved melts (e.g., Frets et al. 2013, Tholen et al. 2023). The nature of the fluid – hydrous melt or aqueous Si-bearing fluid – cannot be determined based on the petrological observations alone and will be further discussed on the next section, based on thermodynamical modelling. The protomylonites record no first order change in modal composition relative to the coarse-porphyroclastic peridotites (Figure 4), but display evidence for remobilization of the existing phases, in particular orthopyroxene (and olivine), and crystallization of minor amounts of amphibole in the matrix (Figure 5c,d, 6c). The decrease in recrystallized olivine grain sizes (Figure 3) suggests deformation under higher stresses (75-112 MPa with an average at 93 MPa, Figure 15, Supplementary Material Table S1) relative to that involved in the pervasive and is consistent with the lower equilibration temperatures (800-900°C) recorded by the rims of orthopyroxene crystals in protomylonitic peridotite 85ZA37 (Figure 13d).

Progression of the localized deformation is recorded by a gradual increase in the matrix fraction in the mylonites and ultramylonites (Figure 2, 3, 5e-i, 8). Dislocation creep and dynamic recrystallization play an essential role in the deformation of olivine, as documented by the progressive replacement of the porphyroclasts by recrystallized grains (decrease in size and number of porphyroclasts, Figure 8a) and by the increasing dispersion of the CPO (Figure 10). In the mylonites of the southern massif, plagioclase also dynamically recrystallizes, with an increase in X_{Ca} of the neoblasts relative to the porphyroclasts (Figures 8c,d), which records the decrease in confining pressure (Figure 13d). Evidence for dissolution-precipitation and hydration reactions is omnipresent in the mylonites and ultramylonites. It encompasses: (1) decrease in the size and increase in the shape factor of orthopyroxene porphyroclasts (Figure 8c), (2) increasing fractions of fine-grained orthopyroxene, and to a lesser extent clinopyroxene, with interstitial or film-like habitus in the fine-grained mylonitic matrix and along recrystallized planes that crosscut obliquely, forming C' planes, olivine porphyroclasts (Figures 2, 5e-i, 8a,c,e), and (3) increasing amphibole fractions that progressively replace clinopyroxene and plagioclase in the recrystallized matrix (Figures 2, 5e-i, 8a,c,e). Dissolution and precipitation are also active during deformation at the brittle-ductile transition as attested by the fractures in olivine filled by fine-grained orthopyroxene in ultramylonite 85ZA71-13 (Figure 8e). Plagioclase remains nevertheless a common phase both as porphyroclasts and neoblasts in the matrix in mylonites from the southern massif (Figures 3, 5e, 8c, Table 1). Plagioclase also occurs as small grains rimming spinel in most mylonites from the central and

northern massifs (Figures 3, 5g, 8a, Table 1). In contrast, the ultramylonites have almost no plagioclase and only relicts of clinopyroxene (Figures 3, 5i, 8a, Table 1).

Evolution from protomylonites to mylonites is accompanied by a minor, but not systematic decrease in the average recrystallized grain sizes of olivine (Figure 2). Recrystallized olivine in the ultramylonites has also similar average sizes as in the mylonites. This implies that, despite the decrease in temperature and pressure conditions of the deformation, recorded by the data on rims and matrix grains of mylonites and ultramylonites (<500-850°C, 6.5-1.5 GPa, Figure 13d), and increasing strain localization, stresses did not increase, remaining below 110 MPa (Figure 15).

Olivine crystal preferred orientations in the mylonites and most ultramylonites (Figure 11) corroborate that, despite the presence of fluids along grain boundaries, the activation of dissolution-precipitation processes, and the decreasing temperature conditions, olivine deformed by dislocation creep with dominant activation of the [100](010) slip system. The higher dispersion of the olivine CPO relative to that in the coarse-porphyroclastic peridotites and protomylonites (Figure 10) is consistent with the increase in recrystallized fraction (e.g., Falus et al. 2011). Only four amphibole-rich samples show CPO suggesting similar contributions of [100] and [001] glide to olivine deformation: mylonite 85ZA51 and ultramylonites 85ZA43b and 85ZA31b, in which olivine is almost completely recrystallized, and ultramylonite 85ZA71-13 in the southern massif, which displays evidence for deformation at the brittle-ductile transition (Figure 8e). Ultramylonites 85ZA31b and 85ZA71-13 are characterized by maxima of both [100] and [001] parallel to the lineation and to the maximum of [001] of amphibole (Figure 11), suggesting activation of both [100](010) and [001](010). Ultramylonite 85ZA43b has [100] and [001] maxima normal to the amphibole [001] maximum (Figure 11). Note that the lineation in this ultramylonite is poorly defined. An increase in the contribution of [001] glide to the deformation may result from an increase in stress during deformation during decreasing temperature conditions (e.g., Durham and Goetze 1977, Demouchy et al. 2013). Incorporation of H⁺ in olivine may also favour [001] glide (e.g., Katayama et al., 2004), but at much higher pressures and stresses than those inferred for the deformation of the Zabargad peridotites. Moreover, the H⁺ solubility in olivine at low pressures and temperature conditions is very low (Demouchy and Bolfan-Casanova 2016, Padrón-Navarta and Hermann, 2017). A possible explanation, already proposed to explain [001]-glide olivine CPO in ultramylonites with similar microstructures (Hidas et al. 2016), development of axial-[010] olivine CPO in peridotites deformed in the presence of melts (Higgie and Tommasi 2012, 2014), or of [001] glide CPO in experimental deformation of olivine+basalt systems (Holtzman et al 2003) is that the presence of a fluid phase along grain boundaries may induce additional rotation components and favour orientation of the olivine [001] axis in the flow direction. The fact that in the present study such olivine CPO are only observed in ultramylonites with high amphibole contents and almost no plagioclase suggests that instantaneous fluid fractions have to be rather high for this process to be activated.

The pyroxenes CPO are more variable (Figure 11). Parallelism between the pyroxenes [001] and the olivine [100] maxima suggests deformation by dislocation glide, consistently with the observed undulose extinction and, for the orthopyroxenes, elongation of the porphyroclasts in

some mylonites. However, some mylonites and ultramylonites show pyroxene CPO with a concentration of [001], which is the only possible glide direction in pyroxenes (cf. Frets et al. 2012 and references therein), at high angle to the foliation. These CPO are similar to those described in peridotite mylonites and ultramylonites deformed in presence of aqueous fluids by Hidas et al. (2016). In dissolution-precipitation creep, CPO development may be controlled by epitaxy. However, our data do not show any consistent orientation relation between olivine and pyroxenes CPO. The plagioclase CPO in the mylonites and ultramylonites is much weaker and in most cases different from that in the coarse-porphroclastic peridotites. The change in CPO pattern is associated with the development of a marked substructure and dynamic recrystallization, suggesting that it is due to deformation by dislocation creep with the activation of multiple slip systems.

In conclusion, analysis of the microstructures and CPO in the mylonites and ultramylonites indicates that dislocation creep played an essential role in deformation in the localized shear zones. It also documents that, except in the final stages of this deformation recorded in the ultramylonites, olivine deformed by activating the same slip systems that during deformation in the asthenosphere of deep lithospheric mantle. Evidence for dissolution-precipitation processes, indicating local fluid saturation, is, nevertheless, omnipresent. Fluids play a major role in the mechanical behaviour of the peridotites in the shear zone by (1) allowing deformation of the pyroxenes by dissolution-precipitation creep, (2) creating, via dissolution-precipitation, a fine-grained polymineralic matrix in which grain growth will be hindered by pinning, and (3) lubricating the grain boundaries within this matrix. These fluid-assisted processes allow for deformation to continue at decreasing temperature conditions and faster strain rates (localization implies accommodating the same displacement gradient in a smaller volume) without a major increase in stress. However, the fact that the olivine recrystallized fraction continuously increased until it represented ~50 % of the olivine volume implies that dislocation creep remained important even in the ultramylonites. This suggests that instantaneous fluid fractions remained low and that grain size reduction did not suffice to produce a switch to a deformation dominated by grain boundary sliding. One may also speculate that dissolution-precipitation creep did not play a more important role in the deformation because of the limited solubility of olivine and pyroxenes in aqueous fluids at temperatures < 900° C (Newton and Manning 2002, Macris et al. 2020).

Thermodynamical modelling: constraints on the evolution of the pT conditions and melts or free fluids contents during deformation

To constrain the composition and amount of fluids involved in the different stages of deformation, we run thermodynamical models, which estimate the sequence of mineral reactions and mineral compositional changes in a system with a whole-rock composition representative for the Zabargad peridotites (cf. Supplementary Material Figure S3). These models were run under the assumption of thermodynamic equilibrium along the decompression paths inferred for: (1) the southern massif and (2) the central and northern massifs. The challenge was to model an open system relative to the H₂O component. Indeed, except for the

water responsible for low amounts of high-Ti pargasite observed in the coarse-porphyroclastic peridotites from the central and northern massifs, the petrostructural data in this study imply that externally derived aqueous fluids (here treated as an external H₂O influx) have infiltrated the deforming peridotites either continuously or discontinuously during the decompression. Depending on the PT conditions, this external H₂O influx should lead to reactions producing amphibole and consuming plagioclase and clinopyroxene until hydrous melting or saturation with an aqueous fluid was reached. However, the strong assumption of complete thermodynamic equilibrium with the external fluid is certainly not fulfilled in the natural system. The preservation of core-to-rim compositional gradients, bimodal to multimodal grain size distributions, and contrasting microstructures certificate that complete equilibrium was never achieved, except in the amphibole-rich ultramylonites that record the most localized deformation. The thermodynamic simulations predict therefore minimum local instantaneous fluid contents. Moreover, the thermodynamic modelling was performed using a single representative bulk whole-rock composition. It predicts therefore evolution trends for mineral reactions and mineral compositional changes rather than attempting to reproduce the individual evolution of the diversity of compositions observed in Zabargad peridotites.

The bulk rock composition of sample 85ZA37 was estimated based on modal abundances from EBSD mapping and average mineral chemical compositions from EPMA analyses (cf. Supplementary Material Table 2). Thermodynamic modelling was conducted using oxides with additional O₂ to account for potential redox reactions involving ferric iron. The amount of O₂ component was estimated based on the ferric iron content in spinel inferred by stoichiometry and the spinel modal abundance in 85ZA37, leading to a bulk oxidation state of iron rather conservative ($\text{Fe}^{3+}/(\text{Fe}^{3+}+\text{Fe}^{2+}) = 0.033$ in atom proportions) when compared with that reported by Bonatti et al. (1986) and Piccardo et al. (1988), which ranges from 0.121 and 0.410 with an average of 0.213.

To account for the contrasting PT paths inferred for the southern massif and the central and northern massifs (Figure 14d), pseudosections were computed along two different PT linear decompression trajectories (vertical axis in Figure 16) for a system with variable H₂O content: from strictly dry to 1.0 wt. % bulk H₂O added to the bulk composition of sample 85ZA37 (horizontal axes in Figure 16). Predictions for the evolution of modal and mineral compositions at equilibrium are then presented for nominally dry (200 ppm wt. H₂O) decompression paths (full red and blue lines close to 0 in XH₂O in Figure 17) and two slightly different hydrous decompression paths (red and blue thick lines with a central white line in Figure 16). These hydrous paths diverge from the nominally dry path at 1170 °C for the northern and central massifs and 1100 °C for the southern massif (first appearance of amphibole at near water-undersaturated solidus conditions) and are thereafter constrained by the water-saturated solidus down to ca. 950 °C and 975 °C for northern and central and southern massifs, respectively, and by the presence of a free aqueous fluid at lower temperatures (aqueous fluid saturation). In addition, for the southern massif, we also computed modal and mineral compositions at equilibrium for a melt/aqueous fluid undersaturated path along the near-zero mode of plagioclase (dashed red line in Figure 16) to estimate the plagioclase composition just before its complete replacement.

The nominally dry PT paths correctly reproduce, for instance, the persistence of spinel through the entire decompression path in the central and northern massifs and the occurrence of very coarse (mm-sized) spinel with plagioclase rims in the southern massif peridotites, suggesting that the southern history initially started in the spinel stability field at 0.9 GPa and temperatures around 1150°C (Figure 16). In addition, the very high plagioclase content (up to 15%, but in most samples 5-8%) with clear synkinematic crystallization habitus implies nominally dry initial conditions in the southern massif, since an external influx of only 0.1 wt.% at these conditions would have caused the complete disappearance of plagioclase (Figure 16). In the central and northern massifs, the synkinematic crystallization of websterites, which implies conditions close to the hydrous solidus, and the assemblages of ol + opx + cpx + sp + Ti-rich amphibole, with neither garnet nor garnet pseudomorphs, such as aggregates of opx+cpx+sp, in the coarse-porphroclastic peridotites and websterites constrain initial conditions for the pervasive deformation of at least 1170°C and 1.7 GPa and a bulk H₂O content in the system lower than 0.2 wt. %. The occurrence of orthopyroxene and amphibole in websteritic layers in the north and central massif support the hydrous nature of the melts.

Departure from the nominally dry path during further decompression are however constrained by the microstructural evidence for fluid-assisted deformation. Thermodynamical simulations predict that, at equilibrium, addition of external H₂O to the system systematically results in crystallization of amphibole, with complete replacement of plagioclase (in the north) or of Al-rich spinel (in the central and northern massifs) by amphibole, before reaching conditions at which a free melt or aqueous fluid may exist (Figure 16). At temperature below 840 °C, fluid-saturation conditions further require complete replacement of clinopyroxene leaving a mineral assemblage consisting on olivine + amphibole + Cr-rich spinel in both massifs. The hydrous melt/fluid-saturated decompression paths would have produced essentially the same mineral assemblage in both massifs if equilibrium had been reached continuously during cooling and fluid infiltration, in contrast to the observations. Equilibrium seems, nevertheless, to have been achieved in the ultramylonite 85ZA11, which contains 25 area % of amphibole, almost no clinopyroxene, and has spinels with high Cr contents (compare Figure 16 to Figures 4 and 13). The appearance of a Cr-rich spinel in the ultramylonites of the southern massif constrains the temperatures and pressures in the last deformation stages to < 845 °C and 0.4 GPa and requires instantaneous H₂O contents of at least 0.6 wt %. The absence of chlorite even in the most hydrated samples constrain the minimum temperature of deformation to 700 °C (Figure 16). The preservation of coarse spinels rimmed by plagioclase (in all massifs) and the persistence of plagioclase in the southern massif mylonites requires a spatially heterogeneous fluid distribution and probably heterogeneity of the fluid flux through time, which prevented the reactions to go to completion while still allowing for widespread deformation by dissolution-precipitation.

The observed mineral chemistry trends are also in relatively good agreement with the thermodynamic modelling predictions given the provision that the latter represent the equilibrium compositions towards which the evolution should trend, ignoring any kinetics effects. The comparison between the modelled and observed mineral chemical compositions (Figure 17) may be only made in a qualitative way, because, in addition to the limitation of

partial local re-equilibration, a single bulk rock composition was used as a representative composition to model the mineral composition, whereas the actual Zabargad peridotites show a relatively large compositional range (see Supplementary Material Figure S3).

Under nominally dry conditions, the evolution of orthopyroxene composition is strongly dependent on the decompression and cooling path followed. In contrast, if hydrous decompression paths were followed under complete equilibrium, orthopyroxenes from all three massifs should display similar compositional evolutions (Figure 17a). The fact that different trends in Ca/Al ratios can be still observed (mostly in cores) – with higher ratios in the southern massif and an almost constant Ca content for a range of Al contents in the central and northern massifs – supports initial low H₂O contents and limited re-equilibration of the orthopyroxene porphyroclasts. The similar compositions of the rims and matrix orthopyroxenes in the three massifs are consistent with hydrated systems. The weak decrease in X_{Mg} with decompression and hydration predicted by the models is probably masked in the observations by the variability in X_{Mg} among and within the samples (Figure 17b). Both dry and water-saturated models do consistently predict, however, the increase in and decrease in Al content in clinopyroxenes along the decompression and cooling paths (Figure 17c). It is worth noting, however, that the most recent subsolidus models for orthopyroxene (clinopyroxene) from Tomlinson and Holland (2021) systematically overestimated (underestimated) the Al contents at all conditions relative to the present observations and also through direct comparison with the experimental data of Fumagalli et al. (2017). The same discrepancy is observed if previous suprasolidus models from Jennings and Holland (2015) and Holland et al. (2018) are used.

The observed progressive enrichment in the anorthite component in plagioclase during decompression and cooling (see also Fumagalli et al. 2017) is also correctly modelled, but under nominally dry conditions X_{Ca} never reaches values higher than 0.78 (Figure 17d). Hydrous models predict, however, significant additional enrichment in X_{Ca} under isothermal-isobaric conditions in response to fluid influx (cf. Supplementary Material Figure S4). Anorthitic plagioclases similar to that observed in the matrix of mylonites of the southern massif are predicted to be in equilibrium at temperatures of ~700 °C and ~0.6 wt % H₂O (Figures 16 and 17d). However, under water-saturated conditions, at equilibrium, plagioclase should be fully replaced by amphibole for the entire central/northern path and between 1100–700 °C for the southern path, leading to a gap in the predicted plagioclase anorthite content (Figure 17d). This contrasts with the almost continuous increase in X_{Ca} in plagioclase observed in the Zabargad peridotites, which can be modelled if a melt/aqueous fluid undersaturated path along the near-zero mode of plagioclase (dashed red line in Figure 17) is considered. The composition of the last plagioclase in equilibrium with amphibole under fluid-undersaturated conditions for the southern pT path (cf. Figure 17d). Finally, the X_{Ca} values lower than 0.60 observed in coarse-porphyroclastic peridotites from the central massif (Figure 17d) can only be modelled under nominally dry conditions if whole rock compositions with higher Na₂O/CaO ratios than that of sample 85ZA37 are considered (such as the composition HNaFLZ in Fumagalli et al. 2017). This change in whole rock composition would have the consequence to displace the plagioclase maximum pressure stability up to 0.9 GPa at 1150 °C.

The thermodynamic models predict of a stability gap and sharp increase in the Cr-content and decrease in X_{Mg} in spinel along the H₂O saturated decompression and cooling paths (Figures 16 and 17e). This compositional evolution is consistent with the observations from all three massifs (Figures 13f and 17e). The evolution in the spinel composition is variably recorded in the three massifs, but all samples show a consistent enrichment of Cr-content towards the rims that requires partial re-equilibration with amphibole and therefore external fluid infiltration. An outstanding case is recorded by sample 85ZA50, which displays the most extreme compositional core-rim range (Figure 13f). The absence of the spinel stability gap in the observations may be explained by only partial re-equilibration of the samples during the decompression and cooling paths. Note that the spinel model from Tomlinson and Holland (2021) used in the present thermodynamic models successfully reproduces the Cr evolution trend, but fails to quantitatively reproduce the observed X_{Mg} range with the discrepancy enhanced at the highest Cr-content. This failure might suggest a poor extrapolation of the model to the low temperature conditions inferred for these spinels (<840 °C).

The H₂O saturated decompression and cooling models also reproduce the general observed trend from pargasite to tremolite-rich compositions reflected in the steady decrease in the amphibole occupancy of the A site (Na + K) and the associated linear decrease in Al^{IV} with increasing hydration during decompression and cooling (Figure 17f). However, the model of Green et al (2016) used in the present study systematically overestimates the Al^{IV} content (Figure 17f). The hydrous models also consistently predict a decrease in Ti content in amphibole with decreasing temperature, but the actual Ti contents are strongly dependent on the Ti content in the whole rock and on the amphibole modal content (Figure 17g). Moreover, the amphiboles in Zabargad peridotites show first decrease in Ti with only minor increase in Si content and then increase in Si (i.e., in the tremolite component) under constant a low Ti content (compare Figures 14 and 17g). The amphibole model of Green et al. (2016), which, in contrast to the other models used in this work, was calibrated for mafic systems, is not able to reproduce this two-stage change in Ti vs. Si contents and predicts lower Si contents than the usual ones in pargasite (Figure 17g) calling for new amphibole models for ultramafic compositions.

Implications for the evolution of the Red Sea

The initial deformation in the central/northern and southern massifs records different stages of the rifting process. In both cases, the initial deformation occurred in the presence of melts and is pervasive at the hundreds of meters to the kilometer scale. However, the peridotites of the central and northern massifs record thinning of the subcontinental lithospheric mantle, with deformation initially assisted by reactive percolation of hydrous melts (probably related to the Afar plume) and later by aqueous fluids. The pervasive deformation occurred at temperatures of 1150-1180 °C and pressures of 1.45-1.65 GPa (Figure 16) that is, at depths of 50-70 km in the subcontinental lithosphere, if one considers a 35 km-thick crust. Subsequent thinning and exhumation of this subcontinental lithospheric mantle by shearing in localized shear zones followed a steep, almost isothermal decompression path (Figure 14d). This steep

decompression path is consistent with that recorded by the lower crust gneisses in contact with the peridotites of the central massif (Boudier et al. 1988, Boullier et al. 1997, Seyler and Bonatti 1988). The equilibrated textures of the coarse-porphyroclastic peridotites in these massifs may indicate a time gap between the pervasive and localized deformations, but it could also be explained by fast grain boundary migration, allowing for effective textural re-equilibration during the deformation in presence of hydrous melts (Tommasi et al. 2017). In contrast, the peridotites of the southern massif record mantle exhumation in a more mature system, at the rift-to-drift transition. The pervasive deformation occurred in a shallow <30 km deep lithosphere-asthenosphere boundary, in the presence of melts produced by decompression upwelling in the asthenosphere. The subsequent exhumation of this lithosphere-asthenosphere boundary occurred along a path in which decompression is accompanied by fast cooling.

The final stages of mantle exhumation recorded in the shear zones in all three massifs are marked by an increasing contribution of fluids to the deformation, with increasing amounts of sea water (Figures 13d and 16). This channelling of surface fluids indicates that these shear zones crosscut the entire lithosphere, being connected to brittle faults that attained the surface. The equilibrium conditions recorded in the ultramylonites, including that preserving microstructures typical of deformation at the brittle to ductile transition, indicate that high geothermal gradients and hence that ductile deformation extended up to very shallow depths (700°C at < 0.2 GPa, that is, ~6 km depth). These conditions are equivalent to those expected under an active ridge. The presence of fluids and activation of fluid-assisted deformation processes allowed for increasingly localized deformation at decreasing temperature at roughly constant stresses (Figure 15). The presence of scapolites in the sample deformed at the brittle-ductile transition (Figure 8f) suggests the presence of an evaporitic layer between the peridotites and the sea water during these last stages of deformation. Such a layer might have protected the exhumed peridotites from extensive reaction with seawater, explaining their exceptional freshness (almost complete absence of serpentines).

CONCLUSION

The present study documents thinning and exhumation of the mantle during continental rift and rift-to-drift transition accommodated in extensional shear zones. The petrostructural data in the Zabargad peridotites records both progressive strain localization and fluid-focusing in these extensional shear zones. Coupling of microstructural and petrological analyses enables documenting the full exhumation history of mantle sections up to subsurface conditions at different stages of the rifting process. The central and northern massifs record an evolution starting at depths of 50-70 km in the subcontinental lithospheric mantle (1150-1180 °C, 1.45-1.65 GPa) followed by a steep, almost isothermal decompression path. The southern massif represents a more mature system, at the rift-to-drift transition. Deformation started in a shallow <30 km deep lithosphere-asthenosphere boundary (1100-1200°C, 0.78-0.90 GPa), which was exhumed along a path in which decompression is accompanied by fast cooling.

The association of high-resolution cartography of the microstructure by EBSD with thermodynamic modelling documents the deformation of the olivine load-bearing framework

of the peridotites essentially by dislocation creep, despite the evidence for the presence of, first, melts, and, later, aqueous fluids within the extensional shear zones. The presence of fluids enabled activation of additional deformation processes, such as dissolution-precipitation, which: (1) contributes to deformation by advective transport of matter along stress gradients, (2) reduces strain incompatibility by dissolving ortho- and clinopyroxene, which require higher stresses to deform by dislocation creep than olivine, (3) effectively reduces grain sizes by producing a well-mixed polymineralic fine-grained matrix. In addition, melts and fluids lubricate grain boundaries, enhancing grain boundary mobility and probably, locally, grain boundary sliding.

The evolution of olivine recrystallized grain sizes in the mylonites and ultramylonites indicates that stresses varied little despite the decrease in temperature conditions and the localization of the deformation in smaller and smaller volumes. This points to the progressive weakening of the rocks within the shear zones, which we interpret as due to increasing fluids implication in the deformation. However, the fact that the olivine recrystallized fraction continuously increased implies that dislocation creep remained important even in the ultramylonites, suggesting that fluid-assisted processes alone did not suffice to accommodate the imposed deformation.

The thermodynamic models constrain that decompression and cooling is accompanied by infiltration of increasing amounts of externally derived aqueous fluids. However, the preservation of core-to-rim compositional gradients and, specially, the preservation of plagioclase and clinopyroxene in the mylonites and to a lesser extent ultramylonites suggests that complete thermodynamic equilibrium with the external fluid was never achieved, except in a few ultramylonites. This implies spatially and probably temporally heterogeneous fluid distribution. Despite the limitations of representing the diversity of compositions with a single representative bulk composition and assuming instantaneous equilibrium, the models for H₂O-saturated decompression and cooling paths successfully predict the general evolution trends for the orthopyroxene, clinopyroxene, plagioclase, and amphibole compositions shedding light on the hydration process during decompression and cooling. Systematic discrepancies between modelled and observed compositions highlight, however, limitations in the presently available models for pyroxenes, spinel, and amphiboles in ultramafic systems.

ACKNOWLEDGEMENTS

Françoise Boudier is warmly thanked for generously sharing the samples, photos, field notes, and her knowledge on the Zabargad peridotites. Alain Vauchez is thanked for the multiple discussions on deformation processes. Matthieu Zaderatzky collected the first set of EBSD as part of his Master project at Université de Montpellier under the supervision of AT in 2015. Fabrice Barou, responsible of the EBSD platform at Geosciences Montpellier, acquired the detail EBSD and EDS maps. We also thank Pierre Agrinier and Catherine Mevel for providing the entire amphibole microprobe dataset of Agrinier et al. (1993), as well as Christophe Nevado and Doriane Delmas, Olivia Mauguin, and Anne Delplanque from Geosciences Montpellier,

for the preparation of high-quality thin sections, assistance in the acquisition of the EPMA data, and producing the pseudosection figures, respectively.

FUNDING

This work was supported by the European Research Council (ERC) under the European Union Horizon 2020 Research and Innovation programme [grant agreement No 882450 – ERC RhEoVOLUTION].

REFERENCENCES

- Agrinier, P., Mével, C., Bosch, D. & Javoy, M. (1993). Metasomatic hydrous fluids in amphibole peridotites from Zabargad Island (Red Sea). *Earth and Planetary Science Letters* **120**, 187–205.
- Bachmann, F., Hielscher, R. & Schaeben, H. (2010). Texture Analysis with MTEX – Free and Open Source Software Toolbox. *Solid State Phenomena* **160**, 63–68.
- Bachmann, F., Hielscher, R. & Schaeben, H. (2011). Grain detection from 2d and 3d EBSD data—Specification of the MTEX algorithm. *Ultramicroscopy* **111**, 1720–1733.
- Basch, V., Borghini, G., Fumagalli, P., Rampone, E., Ferrando, C. & Gandolfo, A. (2019). Plagioclase-facies thermobarometric evolution of the External Liguride pyroxenite-bearing mantle (Suvero, Italy). *Ophioliti* **45**.
- Boillot, G. *et al.* (1987). Tectonic denudation of the upper mantle along passive margins: a model based on drilling results (ODP leg 103, western Galicia margin, Spain). *Tectonophysics* **132**, 335–342.
- Bonatti, E. *et al.* (1983). Zabargad (St. John's) Island: an uplifted fragment of sub-Red Sea lithosphere. *Journal of the Geological Society* **140**, 677–690.
- Bonatti, E., Ottonello, G. & Hamlyn, P. R. (1986). Peridotites from the Island of Zabargad (St. John), Red Sea: Petrology and geochemistry. *Journal of Geophysical Research* **91**, 599.
- Boudier, F., Nicolas, A., Ji, S., Kienast, J. R. & Mevel, C. (1988). The gneiss of Zabargad Island: deep crust of a rift. *Tectonophysics* **150**, 209–227.
- Boullier, A.-M., Firdaous, K. & Boudier, F. (1997). Fluid circulation related to deformation in the Zabargad gneisses (Red Sea rift). *Tectonophysics* **279**, 281–302.
- Brey, G. P. & Köhler, T. (1990). Geothermobarometry in Four-phase Lherzolites II. New Thermobarometers, and Practical Assessment of Existing Thermobarometers. *Journal of Petrology* **31**, 1353–1378.
- Brune, S., Kolawole, F., Olive, J.-A., Stamps, D. S., Buck, W. R., Buitter, S. J. H., Furman, T. & Shillington, D. J. (2023). Geodynamics of continental rift initiation and evolution. *Nature Reviews Earth & Environment* **4**, 235–253.
- Bunge (1982). *Texture Analysis in Materials Science*. Elsevier.

- Connolly, J. A. D. (2005). Computation of phase equilibria by linear programming: A tool for geodynamic modeling and its application to subduction zone decarbonation. *Earth and Planetary Science Letters* **236**, 524–541.
- Connolly, J. A. D. (2009). The geodynamic equation of state: What and how. *Geochemistry, Geophysics, Geosystems* **10**, 2009GC002540.
- Dean, S. L., Sawyer, D. S. & Morgan, J. K. (2015). Galicia Bank ocean–continent transition zone: New seismic reflection constraints. *Earth and Planetary Science Letters* **413**, 197–207.
- Demouchy, S. & Bolfan-Casanova, N. (2016). Distribution and transport of hydrogen in the lithospheric mantle: A review. *Lithos* **240–243**, 402–425.
- Demouchy, S., Tommasi, A., Boffa Ballaran, T. & Cordier, P. (2013). Low strength of Earth's uppermost mantle inferred from tri-axial deformation experiments on dry olivine crystals. *Physics of the Earth and Planetary Interiors* **220**, 37–49.
- Dupuy, C., Mével, C., Bodinier, J.-L. & Savoyant, L. (1991). Zabargad peridotite: Evidence for multistage metasomatism during Red Sea rifting. *Geology* **19**, 722.
- Durham, W. B. & Goetze, C. (1977). Plastic flow of oriented single crystals of olivine: 1. Mechanical data. *Journal of Geophysical Research* **82**, 5737–5753.
- Falus, G., Tommasi, A. & Soustelle, V. (2011). The effect of dynamic recrystallization on olivine crystal preferred orientations in mantle xenoliths deformed under varied stress conditions. *Journal of Structural Geology* **33**, 1528–1540.
- Frets, E. C., Tommasi, A., Garrido, C. J., Vauchez, A., Mainprice, D., Targuisti, K. & Amri, I. (2014). The Beni Bousera Peridotite (Rif Belt, Morocco): an Oblique-slip Low-angle Shear Zone Thinning the Subcontinental Mantle Lithosphere. *Journal of Petrology* **55**, 283–313.
- Frets, E., Tommasi, A., Garrido, C. J., Padrón-Navarta, J. A., Amri, I. & Targuisti, K. (2012). Deformation processes and rheology of pyroxenites under lithospheric mantle conditions. *Journal of Structural Geology* **39**, 138–157.
- Fumagalli, P., Borghini, G., Rampone, E. & Poli, S. (2017). Experimental calibration of Forsterite–Anorthite–Ca-Tschermak–Enstatite (FACE) geobarometer for mantle peridotites. *Contributions to Mineralogy and Petrology* **172**, 38.
- Green, E. C. R., White, R. W., Diener, J. F. A., Powell, R., Holland, T. J. B. & Palin, R. M. (2016). Activity–composition relations for the calculation of partial melting equilibria in metabasic rocks. *Journal of Metamorphic Geology* **34**, 845–869.
- Hidas, K., Tommasi, A., Garrido, C. J., Padrón-Navarta, J. A., Mainprice, D., Vauchez, A., Barou, F. & Marchesi, C. (2016). Fluid-assisted strain localization in the shallow subcontinental lithospheric mantle. *Lithos* **262**, 636–650.
- Higgie, K. & Tommasi, A. (2012). Feedbacks between deformation and melt distribution in the crust–mantle transition zone of the Oman ophiolite. *Earth and Planetary Science Letters* **359–360**, 61–72.
- Higgie, K. & Tommasi, A. (2014). Deformation in a partially molten mantle: Constraints from plagioclase lherzolites from Lanzo, western Alps. *Tectonophysics* **615–616**, 167–181.
- Holland, T. J. B., Green, E. C. R. & Powell, R. (2018). Melting of Peridotites through to Granites: A Simple Thermodynamic Model in the System KNCFMASHTOCr. *Journal of Petrology* **59**, 881–900.

- Holland, T. J. B., Green, E. C. R. & Powell, R. (2022). A thermodynamic model for feldspars in KAlSi_3O_8 – $\text{NaAlSi}_3\text{O}_8$ – $\text{CaAl}_2\text{Si}_2\text{O}_8$ for mineral equilibrium calculations. *Journal of Metamorphic Geology* **40**, 587–600.
- Holland, T. J. B. & Powell, R. (2011). An improved and extended internally consistent thermodynamic dataset for phases of petrological interest, involving a new equation of state for solids: THERMODYNAMIC DATASET FOR PHASES OF PETROLOGICAL INTEREST. *Journal of Metamorphic Geology* **29**, 333–383.
- Holtzman, B. K., Kohlstedt, D. L., Zimmerman, M. E., Heidelbach, F., Hiraga, T. & Hustoft, J. (2003). Melt Segregation and Strain Partitioning: Implications for Seismic Anisotropy and Mantle Flow. *Science* **301**, 1227–1230.
- Jennings, E. S. & Holland, T. J. B. (2015). A Simple Thermodynamic Model for Melting of Peridotite in the System NCFMASOCr. *Journal of Petrology* **56**, 869–892.
- Jollands, M. C. & Müntener, O. (2019). Testing Orthopyroxene Diffusion Chronometry on Rocks From the Lanzo Massif (Italian Alps). *Journal of Geophysical Research: Solid Earth* **124**, 7822–7841.
- Katayama, I., Jung, H. & Karato, S. (2004). New type of olivine fabric from deformation experiments at modest water content and low stress. *Geology* **32**, 1045.
- Kurat, G. *et al.* (1993). Petrology and geochemistry of peridotites and associated vein rocks of Zabargad Island, Red Sea, Egypt. *Mineralogy and Petrology* **48**, 309–341.
- Macris, C. A., Newton, R. C., Wykes, J., Pan, R. & Manning, C. E. (2020). Diopside, enstatite and forsterite solubilities in H₂O and H₂O–NaCl solutions at lower crustal and upper mantle conditions. *Geochimica et Cosmochimica Acta* **279**, 119–142.
- Mainprice, D., Bachmann, F., Hielscher, R. & Schaeben, H. (2015). Descriptive tools for the analysis of texture projects with large datasets using MTEX : strength, symmetry and components. *Geological Society, London, Special Publications* **409**, 251–271.
- McKenzie, D. (1978). Some remarks on the development of sedimentary basins. *Earth and Planetary Science Letters* **40**, 25–32.
- Newton, R. C. & Manning, C. E. (2002). Solubility of enstatite + forsterite in H₂O at deep crust/upper mantle conditions: 4 to 15 kbar and 700 to 900°C. *Geochimica et Cosmochimica Acta* **66**, 4165–4176.
- Nicolas, A., Boudier, F. & Montigny, R. (1987). Structure of Zabargad Island and early rifting of the Red Sea. *Journal of Geophysical Research* **92**, 461.
- Nimis, P. & Grütter, H. (2010). Internally consistent geothermometers for garnet peridotites and pyroxenites. *Contributions to Mineralogy and Petrology* **159**, 411–427.
- Padrón-Navarta, J. A. & Hermann, J. (2017). A Subsolidus Olivine Water Solubility Equation for the Earth's Upper Mantle. *Journal of Geophysical Research: Solid Earth* **122**, 9862–9880.
- Piccardo, G. B., Messiga, B. & Vannucci, R. (1988). The Zabargad peridotite-pyroxenite association: petrological constraints on its evolution. *Tectonophysics* **150**, 135–162.
- Seyler, M. & Bonatti, E. (1988). Petrology of a gneiss-amphibolite lower crustal unit from Zabargad Island, Red Sea. *Tectonophysics* **150**, 177–207.

- Styles, P. & Gerdes, K. D. (1983). St. John's Island (Red Sea): a new geophysical model and its implications for the emplacement of ultramafic rocks in fracture zones and at continental margins. *Earth and Planetary Science Letters* **65**, 353–368.
- Tholen, S., Linckens, J. & Zulauf, G. (2023). Melt-enhanced strain localization and phase mixing in a large-scale mantle shear zone (Ronda peridotite, Spain). *Solid Earth* **14**, 1123–1154.
- Tomlinson, E. L. & Holland, T. J. B. (2021). A Thermodynamic Model for the Subsolidus Evolution and Melting of Peridotite. *Journal of Petrology* **62**, egab012.
- Tommasi, A., Langone, A., Padrón-Navarta, J. A., Zanetti, A. & Vauchez, A. (2017). Hydrous melts weaken the mantle, crystallization of pargasite and phlogopite does not: Insights from a petrostructural study of the Finero peridotites, southern Alps. *Earth and Planetary Science Letters* **477**, 59–72.
- Tommasi, A. & Vauchez, A. (2015). Heterogeneity and anisotropy in the lithospheric mantle. *Tectonophysics* **661**, 11–37.
- Van Der Wal, D., Chopra, P., Drury, M. & Gerald, J. F. (1993). Relationships between dynamically recrystallized grain size and deformation conditions in experimentally deformed olivine rocks. *Geophysical Research Letters* **20**, 1479–1482.
- Weinberg, R. F., Regenauer-Lieb, K. & Rosenbaum, G. (2007). Mantle detachment faults and the breakup of cold continental lithosphere. *Geology* **35**, 1035.
- Wernicke, B. (1981). Low-angle normal faults in the Basin and Range Province: nappe tectonics in an extending orogen. *Nature* **291**, 645–648.
- White, R. W., Powell, R. & Johnson, T. E. (2014). The effect of Mn on mineral stability in metapelites revisited: new $a - x$ relations for manganese-bearing minerals. *Journal of Metamorphic Geology* **32**, 809–828.
- Whitmarsh, R. B., Manatschal, G. & Minshull, T. A. (2001). Evolution of magma-poor continental margins from rifting to seafloor spreading. *Nature* **413**, 150–154.
- Witt-Eickschen, G. & Seck, H. A. (1991). Solubility of Ca and Al in orthopyroxene from spinel peridotite: an improved version of an empirical geothermometer. *Contributions to Mineralogy and Petrology* **106**, 431–439.

FIGURE CAPTIONS

Figure 1. Map of the three massifs showing the spatial distribution of studied samples and the orientation of foliations and lineations for both pervasive and localized deformations (after Nicolas et al, 1987). Squares, diamonds, and circles correspond to samples from the southern, central, and northern massifs, respectively. The red-to-blue colour scale reflects the variations in deformation microstructure (cf. Figure 3). Shades of red indicate samples with coarse porphyroclastic microstructures, associated with the initial pervasive deformation. Shades of blue indicate samples from the localized deformation (metric to cm-scale shear zones) with lighter shades indicating higher recrystallized fractions: dark purple symbols mark protomylonites, medium blues, mylonites and light blues, ultramylonites. Point 85ZA71 in the

southern massif is a scree, in which loose rocks with highly variable microstructures were collected.

Figure 2. (a) EBSD phase map and (b) map illustrating the separation of porphyroclasts (purple) from neoblasts (orange) based on the double criteria of a Grain Orientation Spread (GOS) $\geq 1^\circ$ and an equivalent grain diameter $\geq 400 \mu\text{m}$ for a domain of mylonitic peridotite 85ZA45.

Figure 3. (a) Olivine neoblasts area-weighted mean equivalent grain size vs. neoblasts area fraction (relative to the total olivine area fraction). (b) Olivine neoblasts area-weighted mean equivalent grain size vs. orthopyroxene area-weighted mean equivalent grain size. Squares, diamonds, and circles correspond to samples from the southern, central, and northern massifs, respectively.

Figure 4. Modal composition as a function of the bulk (all phases) recrystallized fraction (cf. Figure 2).

Figure 5. Phase maps derived from EBSD data (a,c,e,g,i) and photomicrographs (b,d,f,h) illustrating typical (a,b) coarse-porphyroclastic, (c,d) protomylonitic, (e,f,g,h) mylonitic, and (i, j) ultramylonitic microstructures.

Figure 6. Phase maps derived from EBSD data illustrating details of the (a) coarse-porphyroclastic microstructure in plagioclase-rich peridotite 85ZA1 from the southern massif, (b) cm-scale pyroxenitic layering and coarse-porphyroclastic microstructure spinel-peridotite 86Z30 from the central massif, (c) protomylonitic microstructure in plagioclase and clinopyroxene peridotite 85ZA37 from the southern massif, and (d) sample 85ZA26C from the southern massif with gabbroic to troctolitic composition displaying a coarse-porphyroclastic microstructure crosscut by a amphibole-rich vein.

Figure 7. (a,c,e,g,i) Misorientation relative to the mean orientation of the grain and (b,d,f,h,j) Kernel Average Misorientation (KAM) maps depicting the internal deformation of the grains in the different microstructural groups. High KAM values materialize the subgrain boundaries. Tones of red = olivine, blue = orthopyroxene, green = clinopyroxene, yellow = plagioclase, purple = spinel, and cyan = amphibole. Grain boundaries (misorientations $> 15^\circ$) in black.

Figure 8: Phase maps derived from EBSD data (a,c,e) and compositional maps derived from EDS data (b,d,f) illustrating microstructurally controlled variations in mineralogic composition in mylonites (a-d) and ultramylonites (e,f). (b) Ti map documenting two generations of amphibole replacing clinopyroxene: coarse grains with high Ti contents surrounded by finer-grained Ti-poor amphiboles, in mylonite 85ZA45 of the northern massif. (d) Ca+Na maps with red to blue tones documenting the increase in anorthite content in plagioclase from the core of porphyroclasts to the recrystallized grains in mylonite 95ZA7b

of the southern massif. (e) Cl map in which cyan tones document the occurrence of two generations of scapolite with different Cl-contents in ultramylonite 85ZA71-13 of the southern massif.

Figure 9. Statistical microstructural data for olivine and orthopyroxene porphyroclasts: (a) grain size, defined by the equivalent grain diameter, (b) elongation, defined by the aspect ratio, (c) shape, defined by the shape factor, and (d) internal deformation, defined by the mean grain orientation spread (GOS). The values displayed are area-weighted averages over the entire EBSD map scale. This averaging was chosen to avoid over-representation of the numerous small grains that occupy in most cases a limited surface of the thin section. Legend as in Figure 1: squares = Southern massif, circles = Central massif; diamonds = Northern massif; redish symbols = coarse-porphyroclastic samples; bluish symbols = LT protomylonites to ultramylonites, with the transparency increasing with increasing neoblasts proportion. The dashed line marks the 1:1 relation.

Figure 10. Olivine crystal preferred orientation symmetry (quantified by the BA index) vs intensity (quantified by J index): (a) Average values over the entire olivine population and (b) average values for porphyroclasts (coarse symbols) and neoblasts (small symbols); data for the same sample are linked by a line. Inset in (b) illustrates the difference in crystal preferred orientation of olivine between porphyroclasts and neoblasts (mean orientation of the grain) for a representative sample. Stereographic projections in the structural reference frame; contours at 1 multiple of a uniform distribution intervals.

Figure 11. Crystal preferred orientations of the main rock-forming minerals in samples representative of the different deformation facies in the (a) central and northern massifs and (b) southern massif. Contoured lower hemisphere stereographic projections in the structural reference frame (X is the lineation and Z the normal to the foliation) of all measurements in the map. Contours at 1 multiple of a uniform density intervals. Pie diagrams on the right show the modal composition of the samples (color legend as in the phase maps in Figure 6: olivine = red; orthopyroxene = blue; clinopyroxene = green; plagioclase = yellow; amphibole = cyan; spinel = purple) with the hatched portion representing the porphyroclasts' area fraction for each mineral.

Figure 12. Compositions of olivine, orthopyroxene, clinopyroxene, plagioclase, and spinel in atoms per unit formula. Symbols indicate the type of analysis: core, intermediate, or rims of porphyroclasts, neoblasts within the fine-grained matrix, or inclusion within another mineral phase. Warm colors indicate samples from the southern massif, greens, samples from the central massif and blues, samples from the northern massif. Lighter tones indicate more recrystallized samples.

Figure 13. Compositions of amphiboles in atoms per unit formula. Symbols indicate the type of analysis: coarse or fine grains in the mylonitic matrix, rims around clinopyroxene or plagioclase, or crystals formed by static replacement in the vicinity of fractures. Warm colors

indicate samples from the southern massif, greens, from the central massif and blues, from the northern massif. Lighter tones indicate more recrystallized samples.

Figure 14. Equilibrium temperature and pressure conditions estimated for the different microstructural assemblages in each sample: cores, intermediate positions, and rims of porphyroclasts or neoblasts from the recrystallized matrix. (a) Al in orthopyroxene (in atoms per formula unit, apfu) vs temperatures estimated using the Al in Opx thermometer, the difference in temperature estimates for similar Al contents between samples from the Central and North massifs and the Southern massif denote the effect of pressure on this thermometer. (b) Ca in orthopyroxene (apfu) vs temperatures estimated using Ca in Opx thermometer. (c) Al_{IV} in clinopyroxene vs X_{Ca} in plagioclase; the experimental data of Fumagalli et al. (2017) used to calibrate the FACE barometer is presented for reference. d. Ca in Opx temperatures vs pressures estimated using the FACE barometer for all plagioclase-bearing microstructural assemblages. In (a) and (b) results of individual analyses are presented (errorbars are smaller than the symbols). In (c) and (d) the uncertainty due to spatial variations in the minerals composition within a sample was estimated by considering all possible combinations between cores, intermediate position, rim and matrix analyses for the different minerals in each sample; it is represented by plotting the median with errorbars representing the dispersion of the estimated values for each microstructural class.

Figure 15. Paleostresses determined based on the mean olivine neoblast equivalent grain size using the piezometer of Van de Wal et al. (1993) for all studied peridotites.

Figure 16. Evolution of the system composition as a function of the water content (X_{H₂O} wt. %) for the pT paths inferred for the northern/central (left, blue) and southern (right, red) massifs for the bulk rock composition of sample 85ZA36, chosen as representative of the average composition of the massif. The full lines on the pseudosections indicate the paths used for calculating the evolution of mineral compositions during exhumation: the simple line marks an almost anhydrous path (100 ppm H₂O), the composite line, a path following the melt or fluid saturation surface, and the dashed line, a melt/aqueous fluid undersaturated path along the near-zero mode of plagioclase. Coloured squares represent the stable modal compositions of the solid matrix: Ol and Opx are not represented because they are stable over the entire field, for the other phases colors as in the phase maps: green = Cpx, yellow = Plg, cyan = Amph, gray = Sp. Garnet, which is not observed in the studied peridotites is indicated in brown. The panels below each pseudosection represent the stability field and modal contents of the four Al-bearing phases. Grey contours in the bottom left of the plagioclase content panel for the southern massif document the stability field and modal content of chlorite.

Figure 17. Comparison between the mineral compositions predicted by the thermodynamical calculations for the four pT-hydration paths and those measured in the Zabargad peridotites. For the calculated compositions, the filling of the symbols indicates the temperature and their contours the nature of the path: black= almost anhydrous, blue=melt or fluid-saturated, with

squares for the northern/central pT path and circles for the southern pT path. Gray circles in Figure 17d indicate the evolution of X_{Ca} along a melt/aqueous fluid undersaturated path along the near-zero mode of plagioclase. For the measured data, symbols as in Figures 11 and 12 with data from the southern massif in black, central massif in gray, and northern massif in white.

Table 1 : Samples provenance (massif + lat/lon, modal composition (area fraction, determined from the EBSD maps covering at least 90% of the thin section with an uncertainty > 1%), deformation facies, total recrystallized fraction, and pT equilibrium conditions.

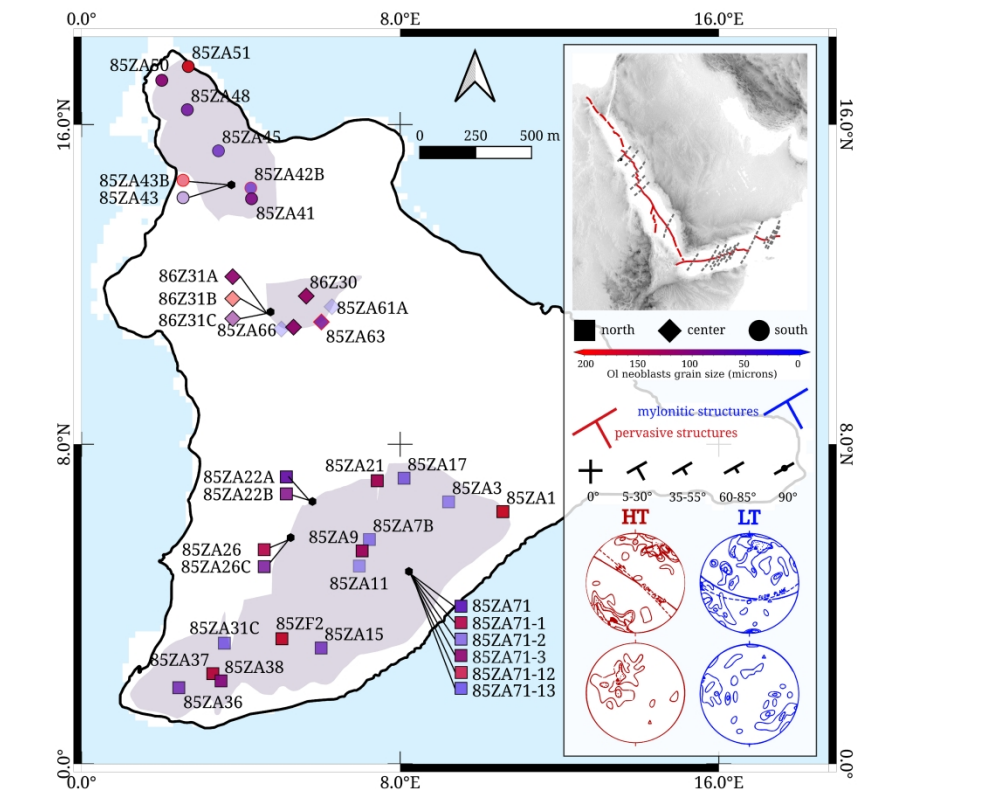


Figure 1. Map of the three massifs showing the spatial distribution of studied samples and the orientation of foliations and lineations for both pervasive and localized deformations (after Nicolas et al, 1987). Squares, diamonds, and circles correspond to samples from the southern, central, and northern massifs, respectively. The red-to-blue colour scale reflects the variations in deformation microstructure (cf. Figure 3). Shades of red indicate samples with coarse porphyroclastic microstructures, associated with the initial pervasive deformation. Shades of blue indicate samples from the localized deformation (metric to cm-scale shear zones) with lighter shades indicating higher recrystallized fractions: dark purple symbols mark protomylonites, medium blues, mylonites and light blues, ultramylonites. Point 85ZA71 in the southern massif is a scree, in which loose rocks with highly variable microstructures were collected.

432x373mm (300 x 300 DPI)

SAMPLES				COORDINATES		COMPOSITIONS (%)						OLIVINE NEOBLASTS	
massif	lithology	facies	sample	longitude	latitude	OI	Opx	Cpx	Plg	Sp	Amph	area fraction (%)	grain size (μm)
center	peridotite	coarse porphyroclastic	86Z30	36°11'35"	23°36'54"	45	29	17	0	0	5	3	104
center	peridotite	coarse porphyroclastic	85ZA65	36°11'32"	23°36'49"	51	19	24	0	1	2	6	102
center	peridotite	coarse porphyroclastic	86Z31A	36°11'29"	23°36'52"	45	34	11	0	1	6	6	115
center	peridotite	mylonite	86Z31C	36°11'29"	23°36'52"	61	17	0	0	0	19	47	98
center	pyroxenite	ultramylonite	86Z31B	36°11'29"	23°36'52"	0	33	49	1	0	13	56	197
center	pyroxenite	ultramylonite	85ZA63	36°11'37"	23°36'50"	3	8	42	11	2	31	77	82
center	pyroxenite	ultramylonite	85ZA61A	36°11'39"	23°36'53"	0	42	1	0	1	54	99	18
center	pyroxenite	ultramylonite	85ZA66	36°11'31"	23°36'49"	0	13	26	0	0	59	100	21
north	peridotite	mylonite	85ZA51	36°11'16"	23°37'30"	81	6	0	0	0	11	15	168
north	pyroxenite	mylonite	85ZA42B	36°11'26"	23°37'11"	0	28	57	2	0	10	18	62
north	peridotite	mylonite	85ZA50	36°11'12"	23°37'28"	69	16	4	0	1	7	22	96
north	peridotite	mylonite	85ZA48	36°11'16"	23°37'24"	66	13	1	0	1	16	35	82
north	pyroxenite	mylonite	85ZA43	36°11'23"	23°37'12"	10	33	0	0	0	55	47	173
north	peridotite	mylonite	85ZA45	36°11'21"	23°37'17"	60	20	2	0	2	15	49	68
north	peridotite	protomylonite	85ZA41	36°11'26"	23°37'10"	61	15	2	0	2	17	4	91
north	peridotite	ultramylonite	85ZA43B	36°11'23"	23°37'12"	60	9	0	0	0	29	66	71
south	peridotite	coarse porphyroclastic	85ZA21	36°11'46"	23°36'25"	66	19	7	4	0	1	6	114
south	peridotite	coarse porphyroclastic	85ZA26	36°11'32"	23°36'16"	73	19	2	1	0	1	6	143
south	peridotite	coarse porphyroclastic	85ZA1	36°12'6"	23°36'20"	62	18	2	13	1	1	7	155
south	peridotite	coarse porphyroclastic	85ZA71-1	36°11'51"	23°36'11"	62	19	6	9	0	1	7	143
south	peridotite	coarse porphyroclastic	85ZA71-3	36°11'51"	23°36'11"	53	0	33	8	0	3	7	113
south	peridotite	coarse porphyroclastic	85ZF2	36°11'31"	23°36'0"	63	24	6	4	0	0	13	152
south	pyroxenite	coarse porphyroclastic	85ZA9	36°11'43"	23°36'14"	35	10	30	6	0	16	14	108
south	peridotite	mylonite	85ZA3	36°11'57"	23°36'22"	45	19	21	9	0	3	16	40
south	peridotite	mylonite	85ZA22B	36°11'35"	23°36'22"	54	24	11	6	0	2	16	98
south	pyroxenite	mylonite	85ZA71-12	36°11'51"	23°36'11"	22	6	30	38	1	1	18	154
south	peridotite	mylonite	85ZA37	36°11'20"	23°35'55"	57	23	9	7	0	0	19	120
south	pyroxenite	mylonite	85ZA26C	36°11'32"	23°36'16"	15	19	32	25	0	7	20	87
south	peridotite	mylonite	85ZA38	36°11'21"	23°35'54"	64	17	7	4	0	5	22	94
south	peridotite	mylonite	85ZA36	36°11'14"	23°35'53"	44	31	11	9	0	1	22	72
south	peridotite	mylonite	85ZA7B	36°11'44"	23°36'16"	52	24	8	9	0	4	39	46
south	peridotite	mylonite	85ZA71-2	36°11'51"	23°36'11"	54	15	0	0	0	29	46	37
south	peridotite	mylonite	85ZA71-13	36°11'51"	23°36'11"	64	24	0	0	0	9	48	36
south	peridotite	protomylonite	85ZA15	36°11'37"	23°35'59"	63	22	7	5	0	0	4	69
south	peridotite	protomylonite	85ZA31C	36°11'22"	23°35'60"	59	13	11	6	0	9	6	54
south	peridotite	protomylonite	85ZA22A	36°11'35"	23°36'22"	72	22	2	0	0	1	8	73
south	peridotite	protomylonite	85ZA71	36°11'51"	23°36'11"	53	27	3	0	0	15	12	61
south	peridotite	protomylonite	85ZA17	36°11'50"	23°36'26"	60	18	7	9	0	3	13	55
south	peridotite	ultramylonite	85ZA11	36°11'43"	23°36'12"	67	8	1	0	0	21	52	35

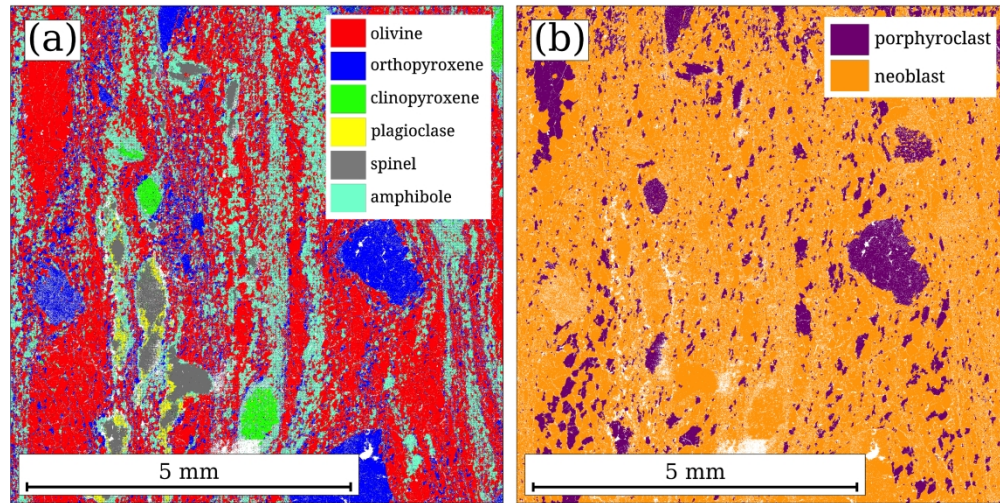


Figure 2. (a) EBSD phase map and (b) map illustrating the separation of porphyroclasts (purple) from neoblasts (orange) based on the double criteria of a Grain Orientation Spread (GOS) $\geq 1^\circ$ and an equivalent grain diameter $\geq 400 \mu\text{m}$ for a domain of mylonitic peridotite 85ZA45.

161x81mm (600 x 600 DPI)

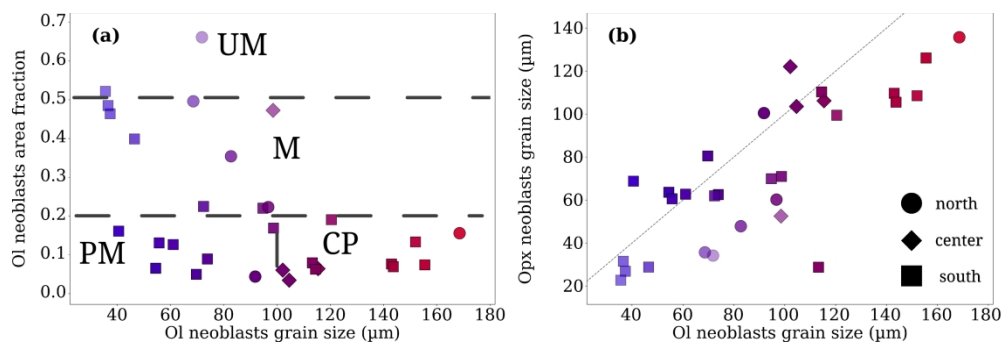


Figure 3. (a) Olivine neoblasts area-weighted mean equivalent grain size vs. neoblasts area fraction (relative to the total olivine area fraction). (b) Olivine neoblasts area-weighted mean equivalent grain size vs. orthopyroxene area-weighted mean equivalent grain size. Squares, diamonds, and circles correspond to samples from the southern, central, and northern massifs, respectively.

161x53mm (600 x 600 DPI)

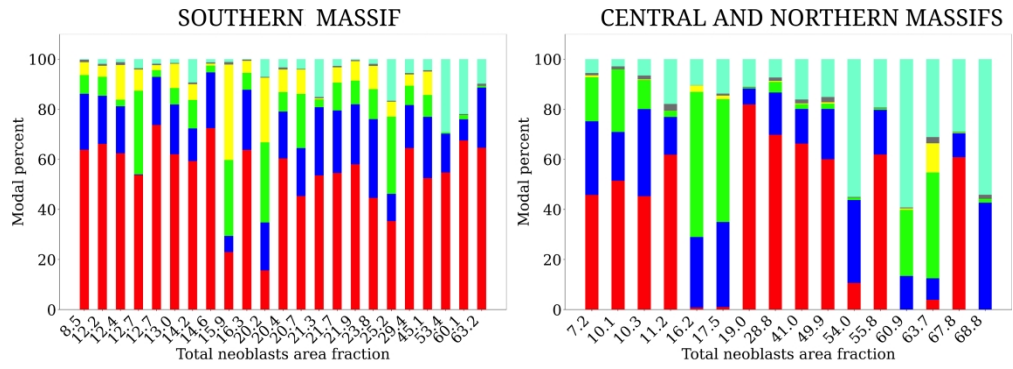


Figure 4. Modal composition as a function of the bulk (all phases) recrystallized fraction (cf. Figure 2).

181x64mm (600 x 600 DPI)

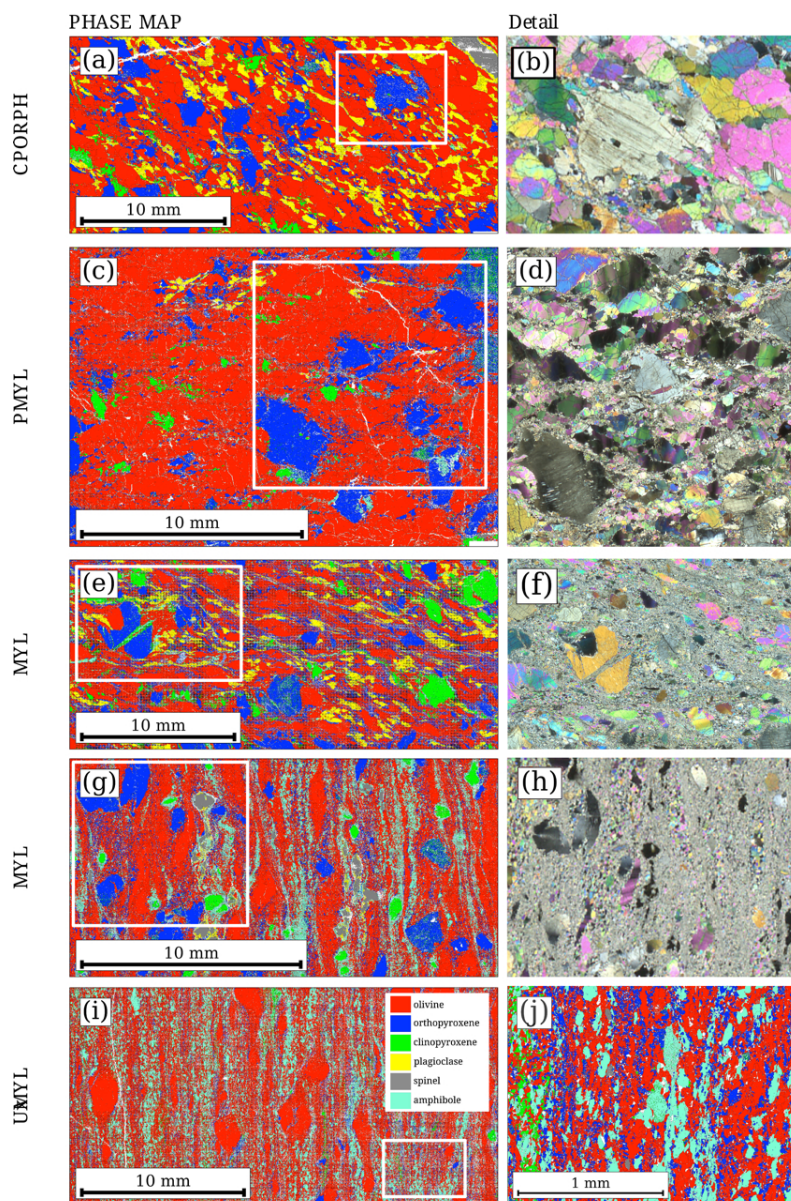


Figure 5. Phase maps derived from EBSD data (a,c,e,g,i) and photomicrographs (b,d,f,h) illustrating typical (a,b) coarse-porphroclastic, (c,d) protomylonitic, (e,f,g,h) mylonitic, and (i, j) ultramylonitic microstructures.

297x451mm (72 x 72 DPI)

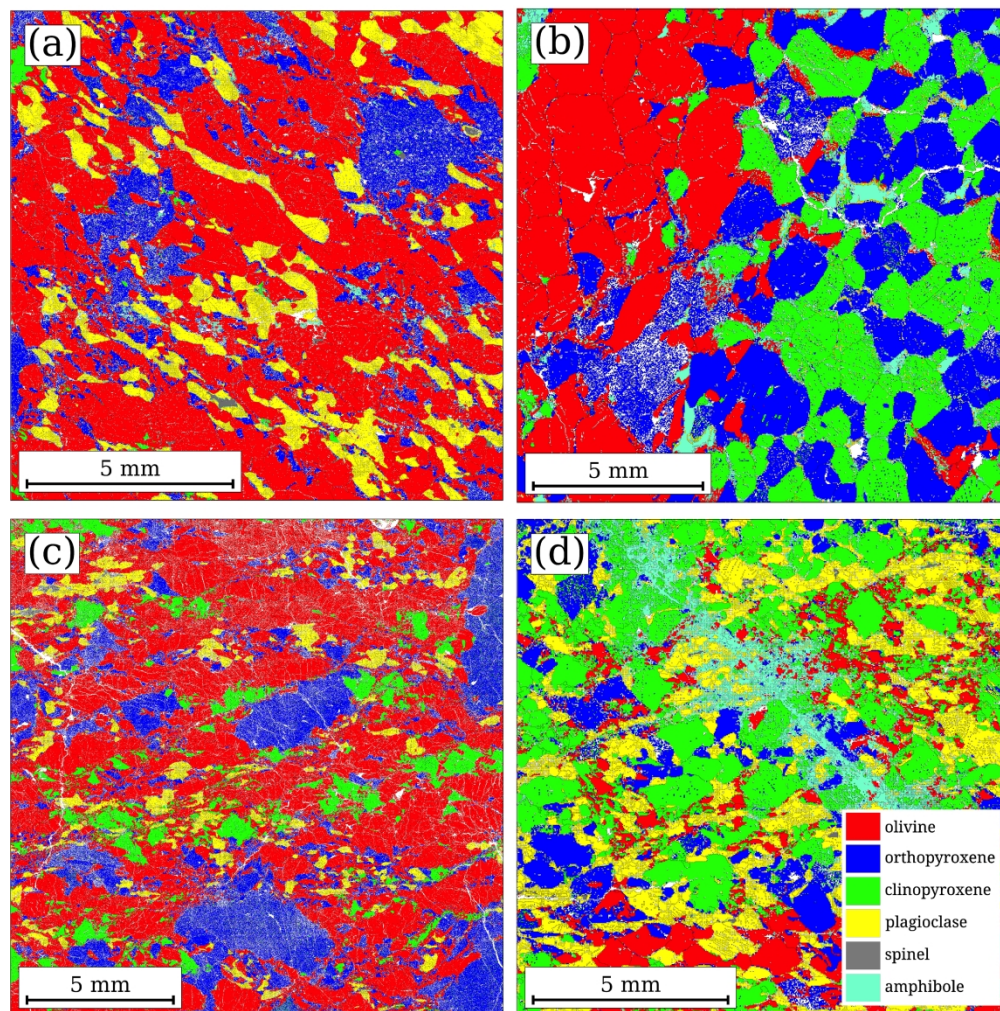


Figure 6. Phase maps derived from EBSD data illustrating details of the (a) coarse-porphyroclastic microstructure in plagioclase-rich peridotite 85ZA1 from the southern massif, (b) cm-scale pyroxenitic layering and coarse-porphyroclastic microstructure spinel-peridotite 86Z30 from the central massif, (c) protomylonitic microstructure in plagioclase and clinopyroxene peridotite 85ZA37 from the southern massif, and (d) sample 85ZA26C from the southern massif with gabbroic to troctolitic composition displaying a coarse-porphyroclastic microstructure crosscut by an amphibole-rich vein.

161x164mm (600 x 600 DPI)

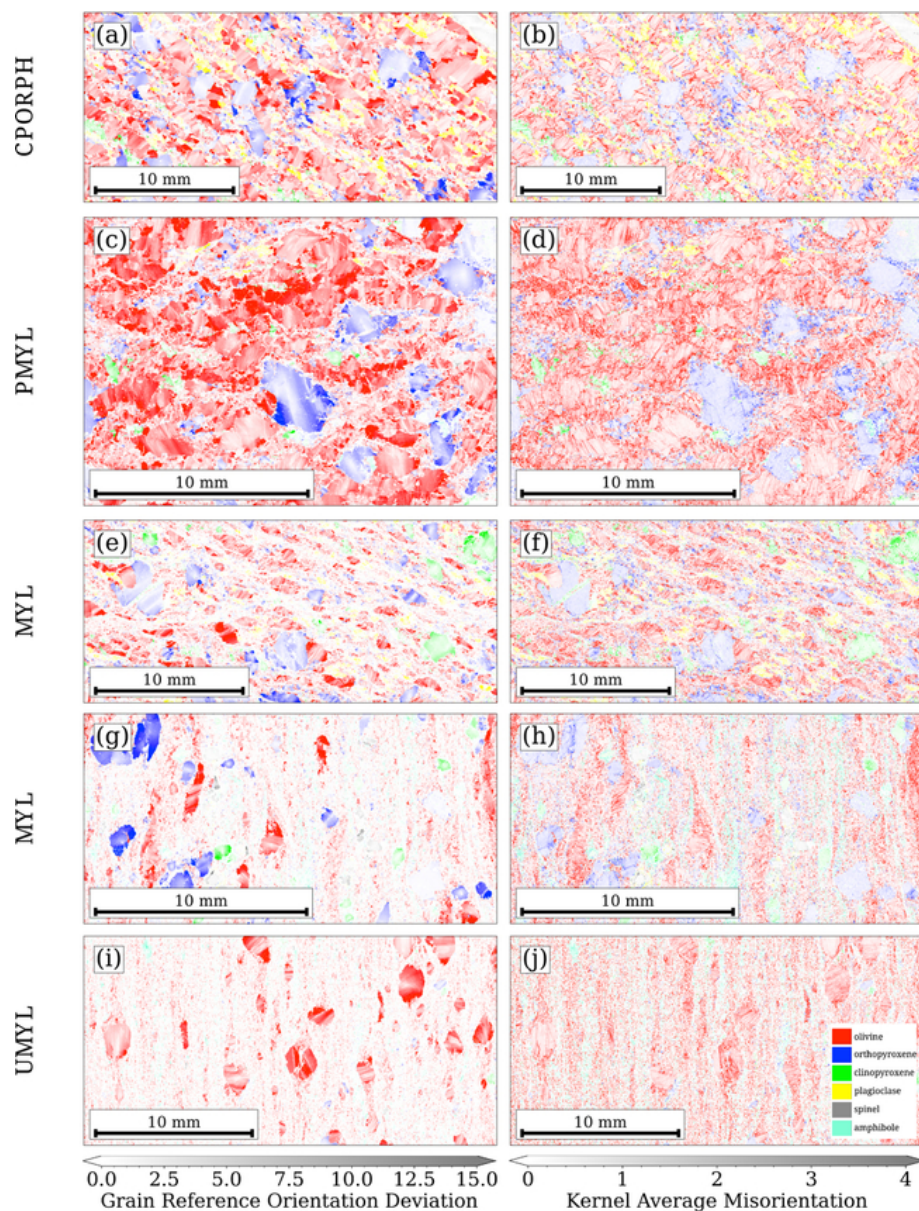


Figure 7. (a,c,e,g,i) Misorientation relative to the mean orientation of the grain and (b,d,f,h,j) Kernel Average Misorientation (KAM) maps depicting the internal deformation of the grains in the different microstructural groups. High KAM values materialize the subgrain boundaries. Tones of red = olivine, blue = orthopyroxene, green = clinopyroxene, yellow = plagioclase, purple = spinel, and cyan = amphibole. Grain boundaries (misorientations > 15°) in black.

27x36mm (600 × 600 DPI)

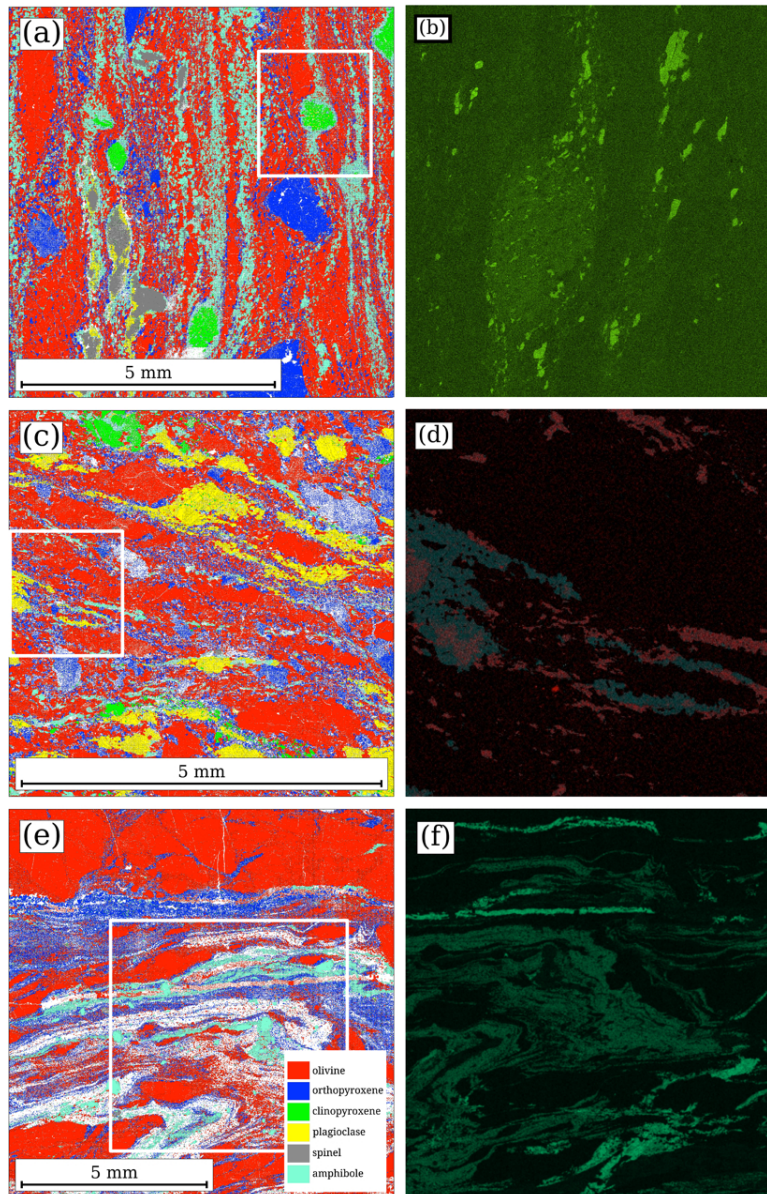


Figure 8: Phase maps derived from EBSD data (a,c,e) and compositional maps derived from EDS data (b,d,f) illustrating microstructurally controlled variations in mineralogical composition in mylonites (a-d) and ultramylonites (e,f). (b) Ti map documenting two generations of amphibole: coarse grains with high Ti contents surrounded by finer-grained Ti-poor amphiboles in mylonite 85ZA45 of the northern massif. (d) Ca+Na maps documenting the decrease in the anorthite content in plagioclase from the core of porphyroclasts to the recrystallized grains in mylonite 95ZA7b of the southern massif. (e) Cl map documenting the crystallization of two generations of scapolite with different Cl-contents in ultramylonite 85ZA71-13 of the southern massif.

293x451mm (72 x 72 DPI)

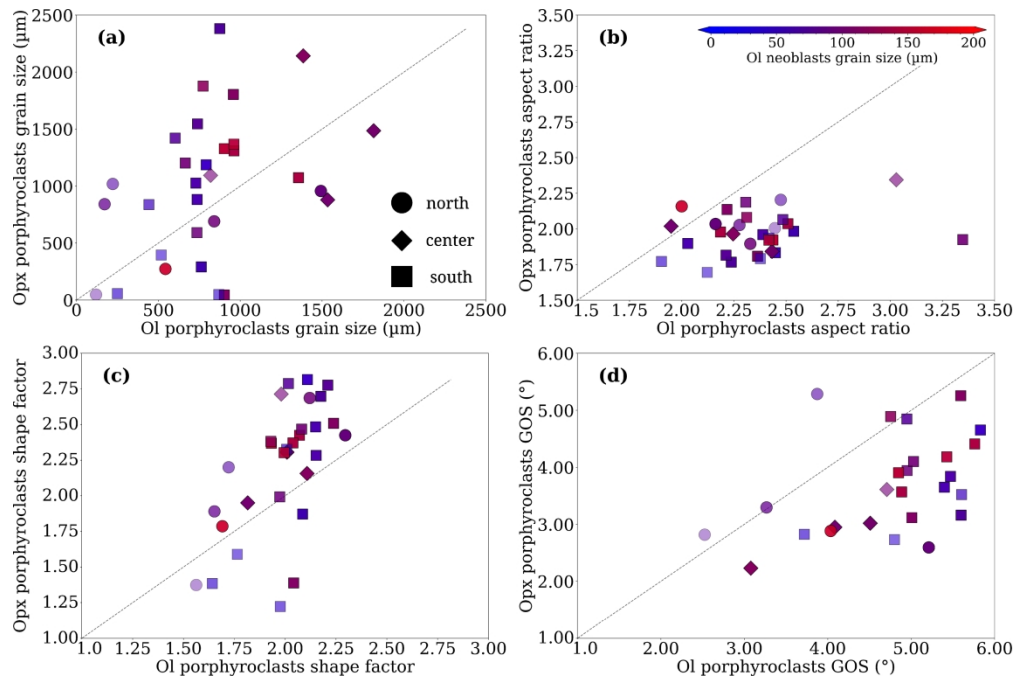


Figure 9. Statistical microstructural data for olivine and orthopyroxene porphyroclasts: (a) grain size, defined by the equivalent grain diameter, (b) elongation, defined by the aspect ratio, (c) shape, defined by the shape factor, and (d) internal deformation, defined by the mean grain orientation spread (GOS). The values displayed are area-weighted averages over the entire EBSD map scale. This averaging was chosen to avoid over-representation of the numerous small grains that occupy in most cases a limited surface of the thin section. Legend as in Figure 1: squares = Southern massif, circles = Central massif; diamonds = Northern massif; redish symbols = coarse-porphyroclastic samples; bluish symbols = LT protomylonites to ultramylonites, with the transparency increasing with increasing neoblasts proportion. The dashed line marks the 1:1 relation.

161x107mm (600 x 600 DPI)

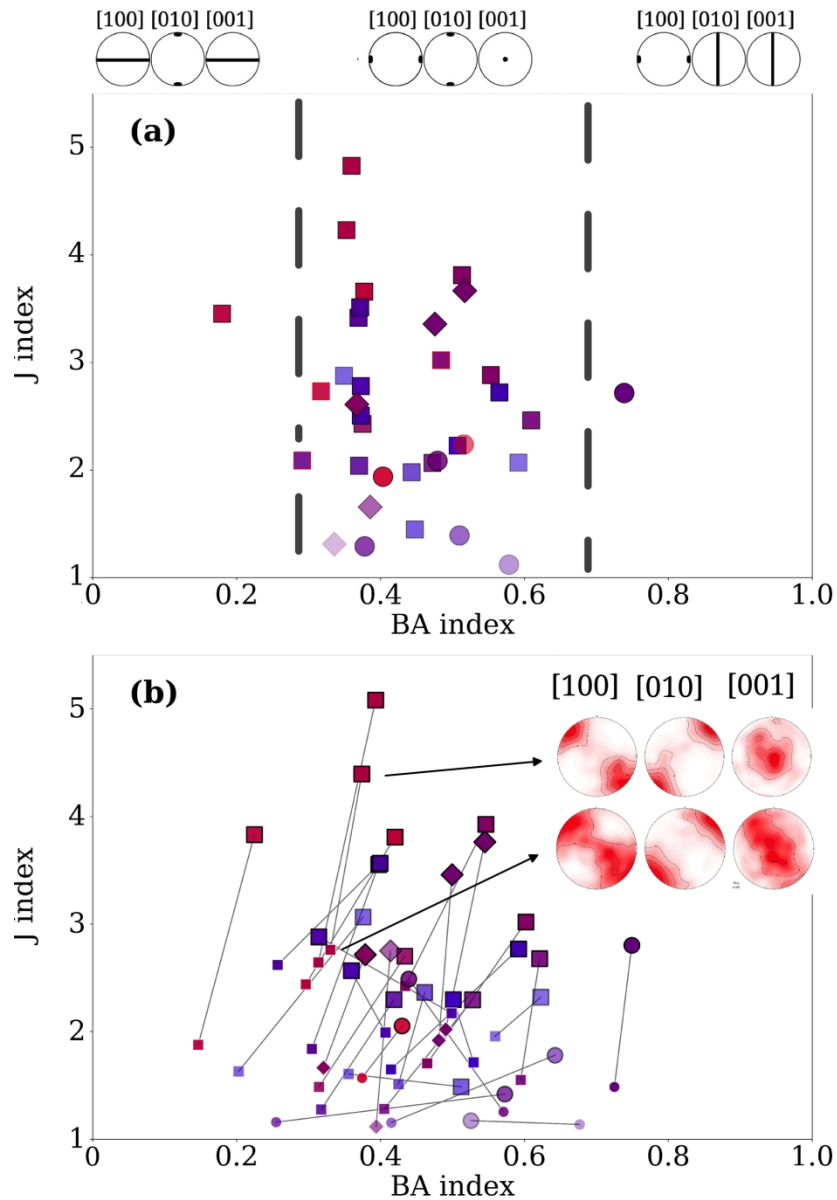


Figure 10. Olivine crystal preferred orientation symmetry (quantified by the BA index) vs intensity (quantified by J index): (a) Average values over the entire olivine population and (b) average values for porphyroclasts (coarse symbols) and neoblasts (small symbols); data for the same sample are linked by a line. Inset in (b) illustrates the difference in crystal preferred orientation of olivine between porphyroclasts and neoblasts (mean orientation of the grain) for a representative sample. Stereographic projections in the structural reference frame; contours at 1 multiple of a uniform distribution intervals.

80x117mm (600 x 600 DPI)

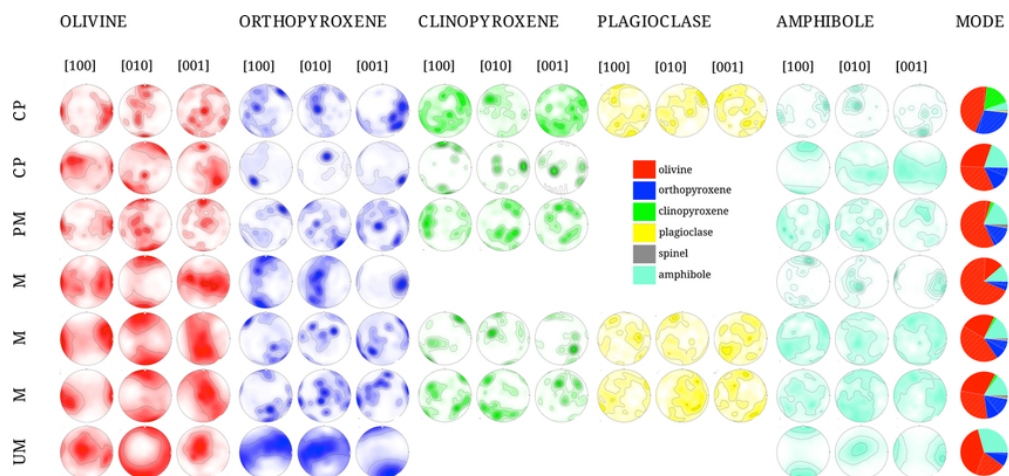


Figure 11a. Crystal preferred orientations of the main rock-forming minerals in samples representative of the different deformation facies in the (a) central and northern massifs and (b) southern massif. Contoured lower hemisphere stereographic projections in the structural reference frame (X is the lineation and Z the normal to the foliation) of all measurements in the map. Contours at 1 multiple of a uniform density intervals. Pie diagrams on the right show the modal composition of the samples (color legend as in the phase maps in Figure 6: olivine = red; orthopyroxene = blue; clinopyroxene = green; plagioclase = yellow; amphibole = cyan; spinel = purple) with the hatched portion representing the porphyroclasts' area fraction for each mineral.

36x18mm (600 x 600 DPI)

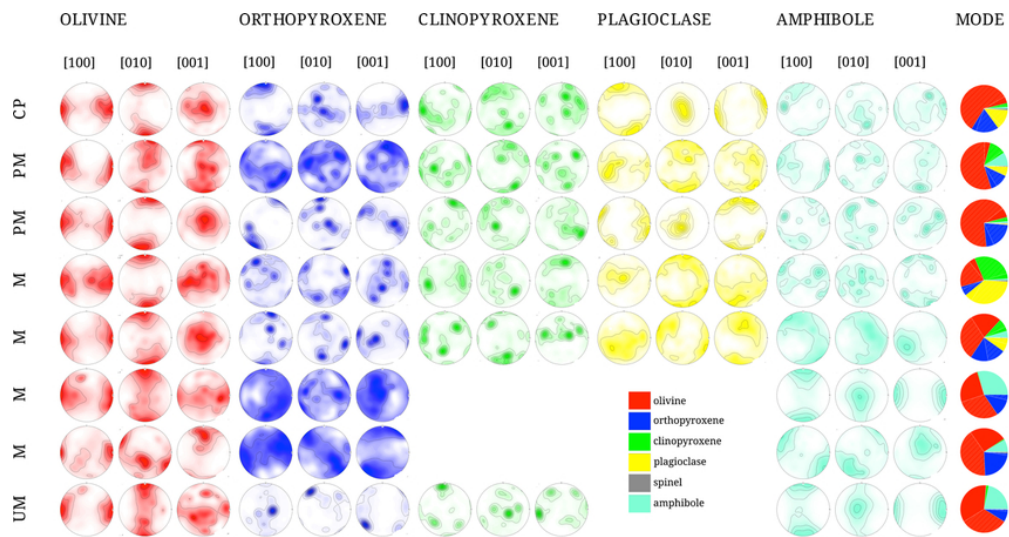


Figure 11b. Crystal preferred orientations of the main rock-forming minerals in samples representative of the different deformation facies in the (a) central and northern massifs and (b) southern massif. Contoured lower hemisphere stereographic projections in the structural reference frame (X is the lineation and Z the normal to the foliation) of all measurements in the map. Contours at 1 multiple of a uniform density intervals. Pie diagrams on the right show the modal composition of the samples (color legend as in the phase maps in Figure 6: olivine = red; orthopyroxene = blue; clinopyroxene = green; plagioclase = yellow; amphibole = cyan; spinel = purple) with the hatched portion representing the porphyroclasts' area fraction for each mineral.

36x18mm (600 x 600 DPI)

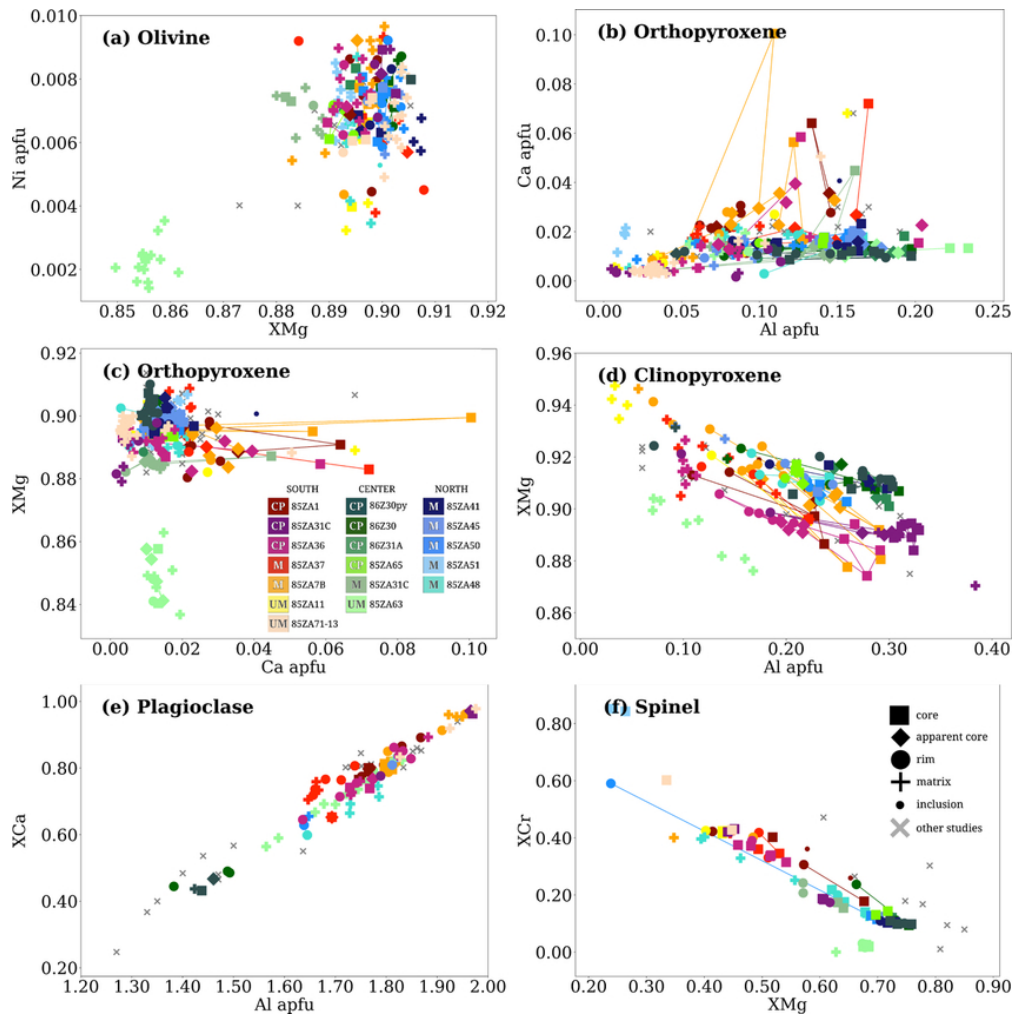


Figure 12. Compositions of olivine, orthopyroxene, clinopyroxene, plagioclase, and spinel in atoms per unit formula. Symbols indicate the type of analysis: core, intermediate, or rims of porphyroclasts, neoblasts within the fine-grained matrix, or inclusion within another mineral phase. Warm colors indicate samples from the southern massif, greens, samples from the central massif and blues, samples from the northern massif. Lighter tones indicate more recrystallized samples.

35x36mm (600 x 600 DPI)

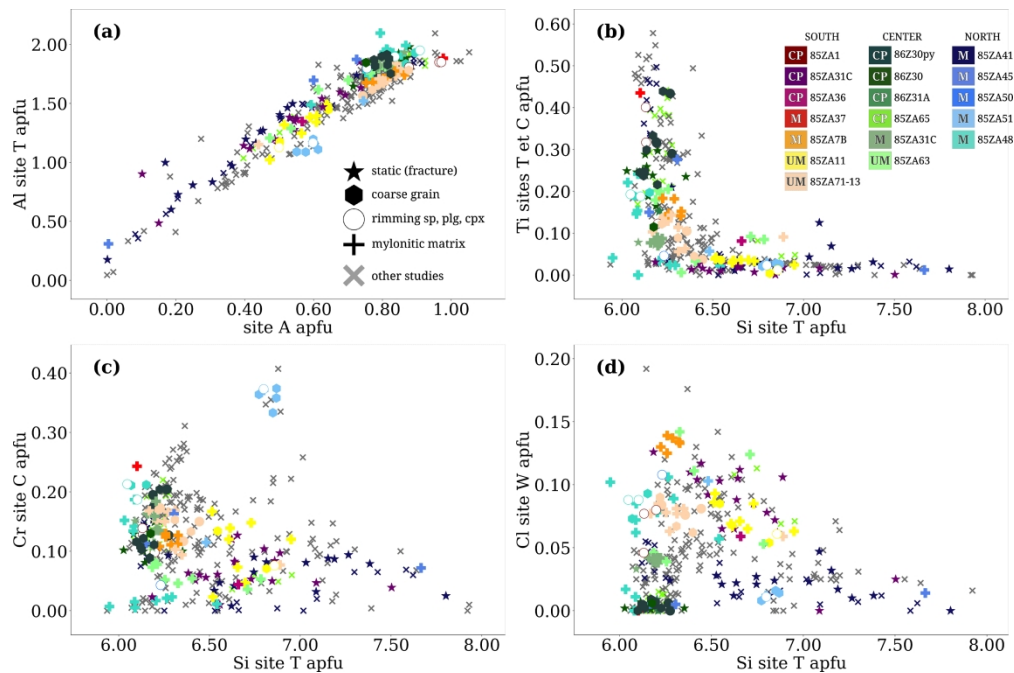


Figure 13. Compositions of amphiboles in atoms per unit formula. Symbols indicate the type of analysis: coarse or fine grains in the mylonitic matrix, rims around clinopyroxene or plagioclase, or crystals formed by static replacement in the vicinity of fractures. Warm colors indicate samples from the southern massif, greens, from the central massif and blues, from the northern massif. Lighter tones indicate more recrystallized samples.

182x121mm (600 x 600 DPI)

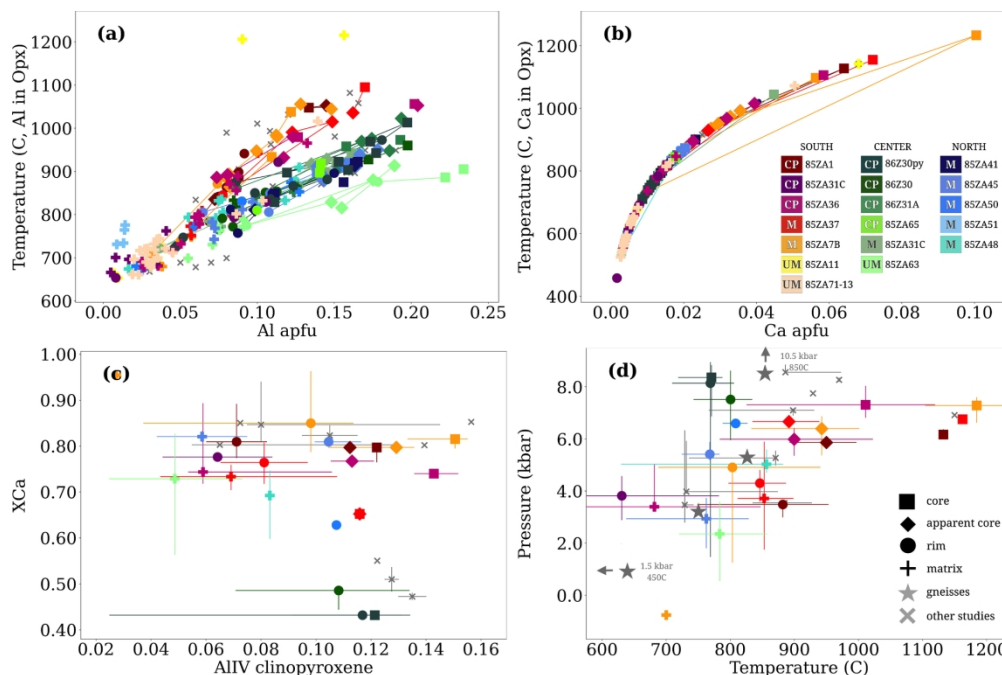


Figure 14. Equilibrium temperature and pressure conditions estimated for the different microstructural assemblages in each sample: cores, intermediate positions, and rims of porphyroclasts or neoblasts from the recrystallized matrix. (a) Al in orthopyroxene (in atoms per formula unit, apfu) vs temperatures estimated using the Al in Opx thermometer, the difference in temperature estimates for similar Al contents between samples from the Central and North massifs and the Southern massif denote the effect of pressure on this thermometer. (b) Ca in orthopyroxene (apfu) vs temperatures estimated using Ca in Opx thermometer. (c) AlIV in clinopyroxene vs XCa in plagioclase; the experimental data of Fumagalli et al. (2017) used to calibrate the FACE barometer is presented for reference. d. Ca in Opx temperatures vs pressures estimated using the FACE barometer for all plagioclase-bearing microstructural assemblages. In (a) and (b) results of individual analyses are presented (errorbars are smaller than the symbols). In (c) and (d) the uncertainty due to spatial variations in the minerals composition within a sample was estimated by considering all possible combinations between cores, intermediate position, rim and matrix analyses for the different minerals in each sample; it is represented by plotting the median with errorbars representing the dispersion of the estimated values for each microstructural class.

181x134mm (300 x 300 DPI)

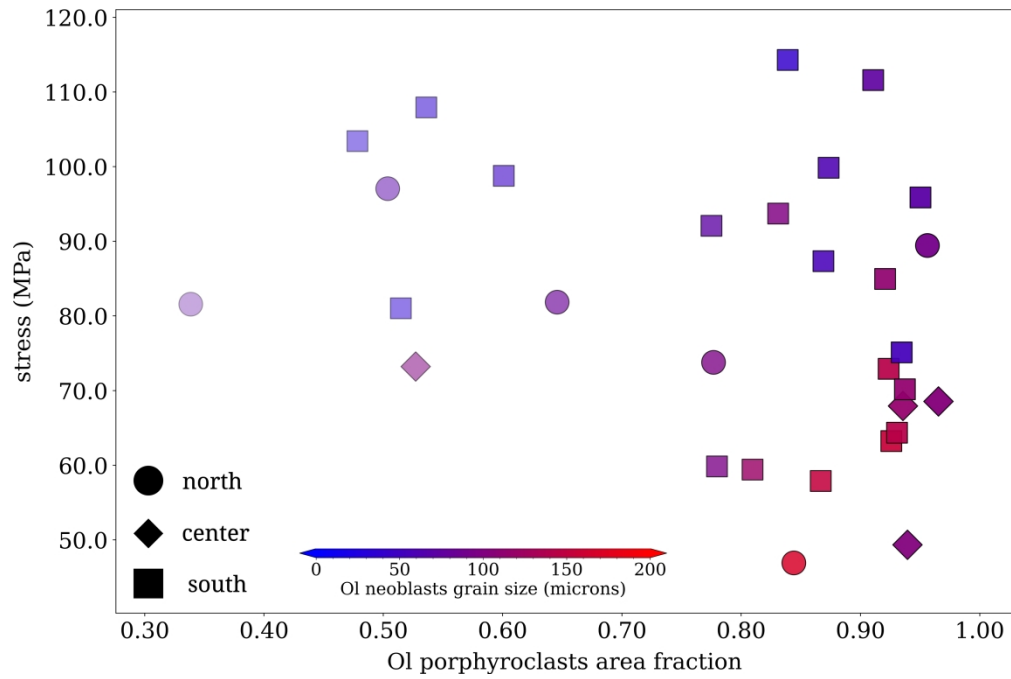


Figure 15. Paleostresses determined based on the mean olivine neoblast equivalent grain size using the piezometer of Van de Wal et al. (1993) for all studied peridotites.

378x251mm (300 x 300 DPI)

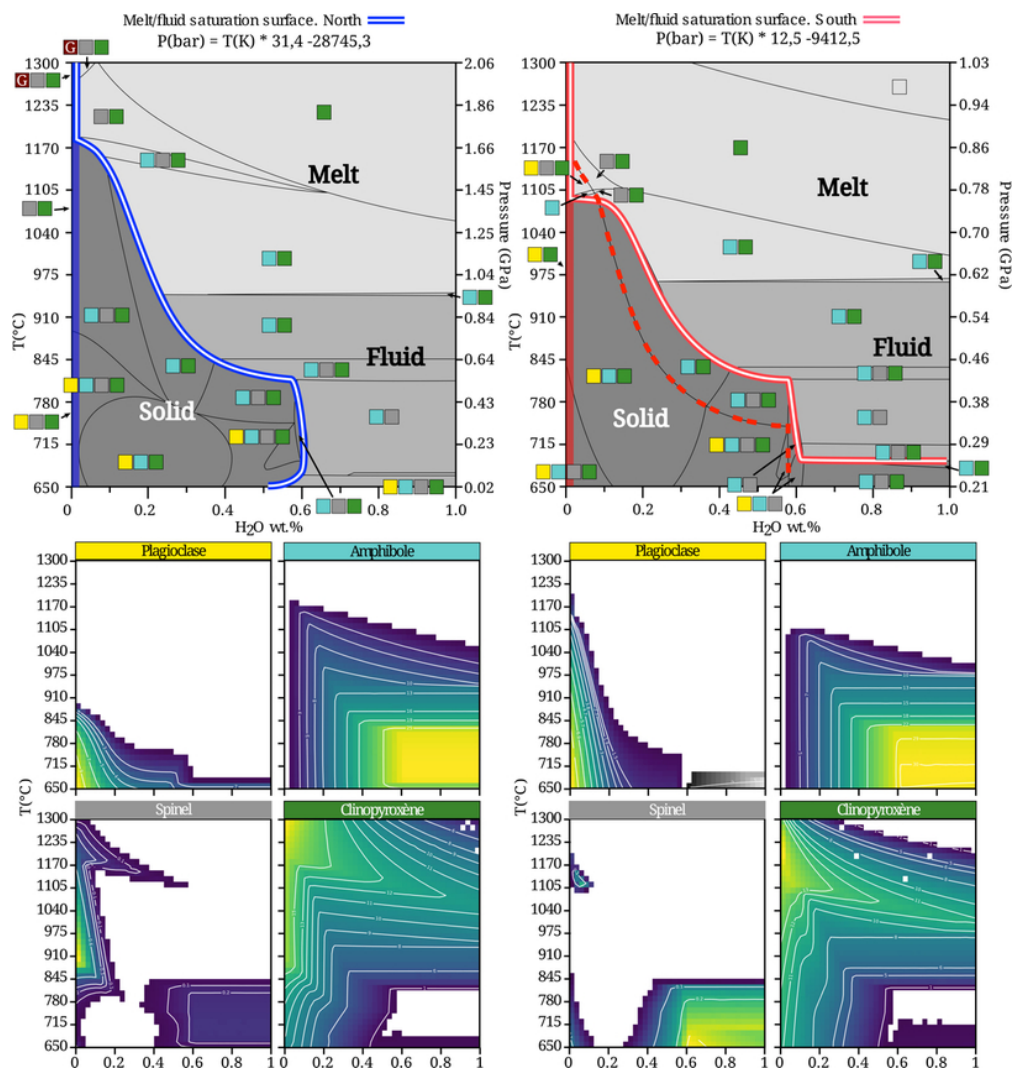


Figure 16. Evolution of the system composition as a function of the water content (XH₂O wt. %) for the pT paths inferred for the northern/central (left, blue) and southern (right, red) massifs for the bulk rock composition of sample 85ZA36, chosen as representative of the average composition of the massif. The full lines on the pseudosections indicate the paths used for calculating the evolution of mineral compositions during exhumation: the simple line marks an almost anhydrous path (100 ppm H₂O), the composite line, a path following the melt or fluid saturation surface, and the dashed line, a melt/aqueous fluid undersaturated path along the near-zero mode of plagioclase. Coloured squares represent the stable modal compositions of the solid matrix: Ol and Opx are not represented because they are stable over the entire field, for the other phases colors as in the phase maps: green = Cpx, yellow = Plg, cyan = Amph, gray = Sp. Garnet, which is not observed in the studied peridotites is indicated in brown. The panels below each pseudosection represent the stability field and modal contents of the four Al-bearing phases. Grey contours in the bottom left of the plagioclase content panel for the southern massif document the stability field and modal content of chlorite.

34x36mm (600 x 600 DPI)

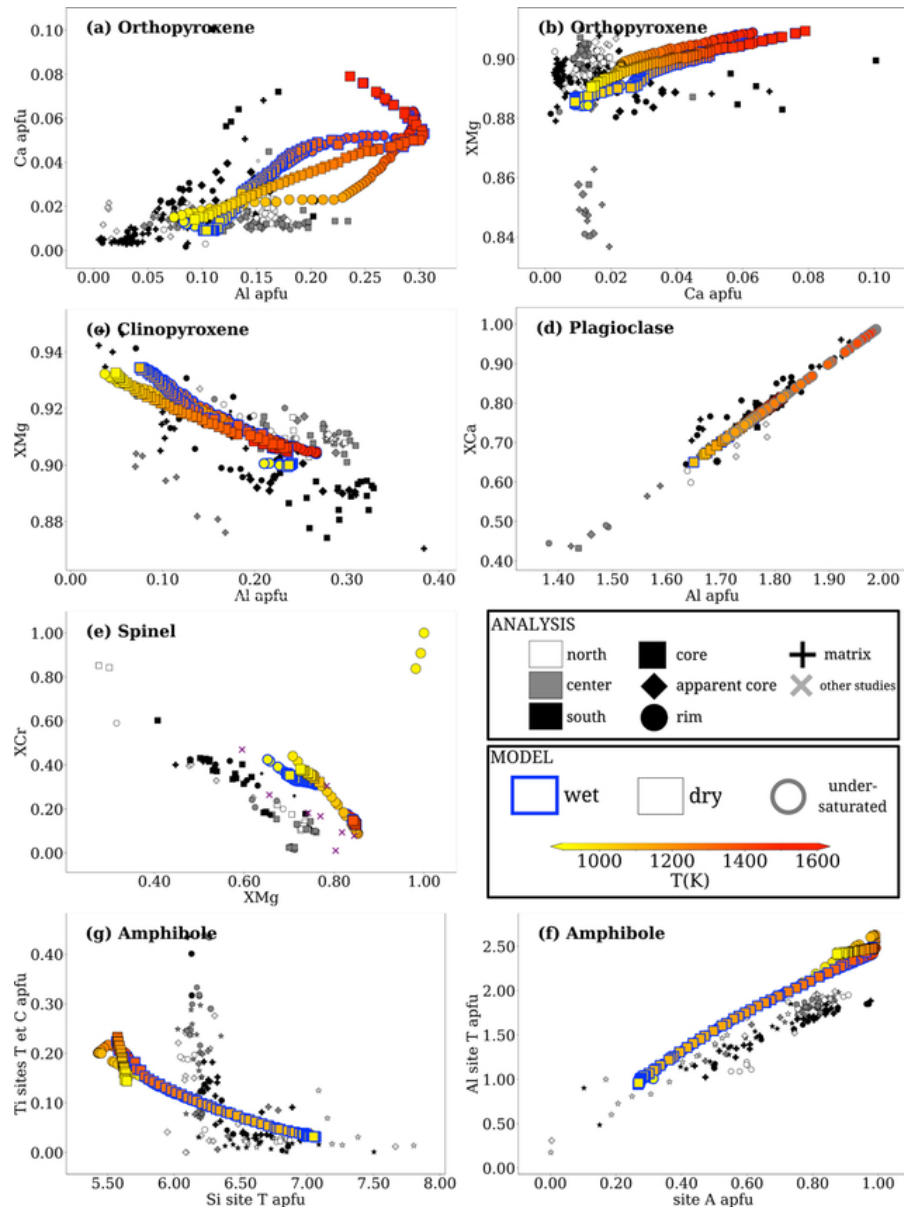


Figure 17. Comparison between the mineral compositions predicted by the thermodynamical calculations for the four pT-hydration paths and those measured in the Zabargad peridotites. For the calculated compositions, the filling of the symbols indicates the temperature and their contours the nature of the path: black= almost anhydrous, blue=melt or fluid-saturated, with squares for the northern/central pT path and circles for the southern pT path. Gray circles in Figure 17d indicate the evolution of XCa along a melt/aqueous fluid undersaturated path along the near-zero mode of plagioclase. For the measured data, symbols as in Figures 11 and 12 with data from the southern massif in black, central massif in gray, and northern massif in white.

27x36mm (600 x 600 DPI)